

# HST $P\alpha$ and $1.9\mu\text{m}$ Imaging of Sgr A West

N. Z. Scoville

Astronomy Department, California Institute of Technology, Pasadena, CA 91125

S. R. Stolovy

SIRTF Science Center, California Institute of Technology, Pasadena, CA 91125

M. Rieke

Steward Observatory, University of Arizona, Tucson, AZ 85721

M. Christopher

Astronomy Department, California Institute of Technology, Pasadena, CA 91125

and F. Yusef-Zadeh

Department of Physics and Astronomy, Northwestern University Evanston, IL 60208

## ABSTRACT

We present HST/NICMOS images at  $0.2''$  resolution (Nyquist sampled in the central  $19''$ ) of the HI  $P\alpha$  emission line in a  $70''$  ( $\alpha$ )  $\times$   $90''$  ( $\delta$ ) region of the Galactic center centered on the non-thermal radio source Sgr A\*. The majority of the emission arises from ionized gas in the mini-spiral in the central parsec.  $P\alpha$  emission is also seen from 26 stellar sources, presumably early-type stars with mass-loss winds. The new data reveal significant small-scale structure ( $\leq 1'' \sim 1.2 \times 10^{17}$  cm) in the ionized gas of the mini-spiral; low surface brightness emission features are also seen for the first time. The ratio of observed  $P\alpha$  emission to 6-cm radio continuum emission is used to derive an extinction map for the ionized gas over the central parsec.  $A_V$  varies from 20 to 50 mag with a median value of  $A_V = 31.1$  mag, in excellent agreement with earlier estimates derived for the stellar sources. Extinctions, independently derived using  $H92\alpha$  recombination line data, were in excellent agreement with those derived from the 6-cm continuum. A broad minimum in the extinction extends  $\sim 30''$  NE–SW over the area of the IRS 16 cluster, including the area of peak flux in  $P\alpha$  and radio continuum. Large increases in extinction are seen along the periphery of the ionized gas, particularly in the direction of the western arm, suggesting that the ionized gas is *partially* extinguished by dust in the molecular clouds at the outside of the ionized region; however the HII cannot be entirely behind the molecular clouds since the extinctions would then be much

greater. The minimum Lyman continuum emission rate within  $40''$  radius of Sgr A\* is  $3.9 \times 10^{50} \text{ sec}^{-1}$  or  $L_{LyC} \simeq 2.7 \times 10^6 L_{\odot}$ , half of this within  $20''$  radius. The small-scale, filamentary structures in the ionized gas have a free thermal expansion time of only  $\sim 3000$  yrs; either magnetic fields or mass-loss winds from the hot emission line stars may contain the ionized filaments. (Eight new emission-line stars were also detected in  $P\alpha$ .)

For both the ionized gas and stellar continuum, the centroids of the emission (corrected for extinction) remain within  $\sim \pm 1''$  from a radius of  $2''$  out to  $40''$ . This provides further evidence that Sgr A\* (the putative central black hole) is indeed at or extremely close ( $\leq 0.04$  pc or  $1.2 \times 10^{17}$  cm) to the center of the Galactic nucleus stellar distribution and presumably the dynamical center of the Galaxy. The  $1.9\mu\text{m}$  surface brightness increases inwards to  $0.9''$  radius and exhibits a decrease or leveling off closer to Sgr A\*, possibly indicating the core radius of the central stellar distribution or depletion of the late-type stars by stellar collisions near the central black hole.

*Subject headings:* Galaxy: center — dust, extinction — infrared: ISM — HII regions

## 1. Introduction

Within the central few parsecs of our Galaxy, radio, infrared and x-ray observations have revealed a massive black hole lying within a region of ionized 'spiral' arms, encompassed by a ring of dense molecular clouds. The black hole is identified with the non-thermal radio source Sgr A\*, and it is estimated to be  $2.6 \times 10^6 M_{\odot}$  from the motions of nearby stars and the neighboring ionized gas (Eckart & Genzel 1996, Genzel *et al.* 2000, Ghez *et al.* 2000). At a projected radius of approximately 2 pc from Sgr A\*, lies the circumnuclear disk/ring (CND) of dense molecular gas and dust clouds (Genzel *et al.* 1985, Güsten *et al.* 1987), and within this ring, ionized gas streams extend down to a few arcsec from Sgr A\* (Lo & Claussen 1983; Lacy *et al.* 1991). The molecular cloud ring can be modelled as a torus (0.5 pc thick) inclined at  $70^{\circ}$  to the line of sight (Jackson *et al.* 1993). Although clearly much less energetic and massive than the luminous AGN seen in many galactic nuclei, this region probably provides our best opportunity to observe in detail the processes associated with buildup of massive black holes and their accretion processes.

Previous studies of the ionized gas in the inner few parsecs of the Galaxy, with an emphasis on the radial velocity kinematics have included observations of [NeII] (Lacy,

Achtermann, & Serabyn 1991),  $\text{Br}\gamma$  (Burton & Allen 1992 and Herbst, Beckwith, & Shure 1993), and  $\text{H}2\alpha$  (Roberts & Goss 1993). Roberts & Goss published a ratio map of their  $\text{H}2\alpha$  radio observations to  $\text{Br}\gamma$  from Burton & Allen (1992) which gave a qualitative representation of the extinction in the inner few parsecs, however, they did not calculate the extinction in  $A_V$ .

We have recently undertaken two investigations aimed at providing the highest resolution imaging of both the ionized and molecular gas in the circumnuclear disk. Most of the existing observations of the ionized and dense molecular gas are at  $\geq 1$  and  $\geq 8$  " resolution, respectively, and thus do not clearly resolve the internal structure of the ionized gas. The molecular gas clouds were imaged in HCN at 3" resolution by Christopher *et al.* (2003) using the Owens Valley mm-Array; here we present HST-NICMOS imaging at 0.2" resolution of the  $1.87\mu\text{m}$   $\text{P}\alpha$  (HI 4-3) recombination emission line. The  $\text{P}\alpha$  line has 12 times greater intrinsic flux than the  $2.16\mu\text{m}$   $\text{Br}\gamma$  line, and thus it provides excellent sensitivity when observed with the NICMOS camera on HST (despite the extra magnitude of extinction at the Galactic center at  $1.87\mu\text{m}$  compared with  $2.16\mu\text{m}$ ). Comparison of the  $\text{P}\alpha$  emission with radio continuum emission from the same ionized gas is used to derive a map of the foreground extinction; previous estimates of the extinction have been mostly derived from the individual stellar colors; the derived extinctions are therefore not spatially continuous and their location along the line of sight is often uncertain. For both the HCN and  $\text{P}\alpha$  observations, multiple fields were observed in order to image the entire Galactic center region out to and including the CND.

In §2, we describe the observations and reduction procedures. Three methods for removing the stellar continuum from the emission line images (scaled subtraction of the 190N image from the 187N image, PSF fitting and subtraction for the bright stars and variable scale factor image subtraction) are discussed in Appendix 1. In §3, we derive the extinction distribution from the observed ratio of  $\text{P}\alpha$  to radio continuum and radio recombination lines and present an extinction-corrected  $\text{P}\alpha$  image. Estimates of the sizes and densities of the HII structures are derived in §4, and the stellar sources with emission line excesses are discussed in §5. We then examine the observed and extinction-corrected diffuse light distribution of stars in §6 and the stellar density profile relative to Sgr A\*.

## 2. Observations and Data Analysis

### 2.1. NICMOS P $\alpha$ Observations

Images of the CND were obtained with the NICMOS camera on HST in the narrow-band 187N (P $\alpha$ ) and 190N filters as part of the NICMOS GTO program. A mosaic image, extending out to 50'' radius, was constructed from four Camera 3 (NIC3) dithered fields and one Camera 2 (NIC2) dithered field (for higher resolution near the center). NIC3 uses a 256 $\times$ 256 HgCdTe array with plate scale of 0.203'' per pixel providing a 52.0'' field of view; Camera 2 has 256 $\times$ 256 0.076'' pixels and a 19.3'' FOV (Thompson *et al.* 1998). The F187N and F190N filters with effective wavelengths of 1.87 and 1.90  $\mu\text{m}$  were used to obtain on-line and off-line images. The F187N filter has a bandwidth of  $\sim 1\%$  corresponding to over 3000km s $^{-1}$ ; it therefore includes all velocities of the Galactic center ionized gas (Lacy *et al.* 1991). The filter also includes a HeI(4-3) doublet line (at 1.8691 and 1.8702  $\mu\text{m}$ ) ; for the extended emission, P $\alpha$  is expected to completely dominate (by more than a factor of 30), but on some emission lines stars (Paumard *et al.* 2001) the HeI line could be a significant contribution.

For each of the field centers (listed in Table 1), 4 dithers were taken spaced by 1.1'' with non-destructive reads at each position (MULTIACCUM). The total integration times for each filter are listed in Table 1. The diffraction limited resolution of HST is 0.19'' at 1.87 $\mu\text{m}$ ; the NIC2 images are therefore sampled at better than the Nyquist frequency but the NIC3 images are undersampled by the Nyquist criterium. Although not completely recovering the Nyquist sampling, the half-pixel dithers do help to reduce the undersampling in NIC3.

### 2.2. Data Reduction

The data were calibrated using the CALNICA version 3.3 task (Bushouse & Stobie 1998) in IRAF<sup>1</sup>/STSDAS with most reference files (static data quality, detector read noise, detector non-linearities files) from the Space Telescope Science Institute (STScI) NICMOS pipeline. The flat-field and dark frames were provided by the NICMOS Instrument Development Team (IDT). The dithered images were then shifted and coadded; for the NIC2 fields, using the the IDP3 routine from the NICMOS IDT software. We estimate the registration accuracy between the NIC2 fields to be better than 0.05 NIC2 pixel. The

---

<sup>1</sup>IRAF is distributed by the National Optical Astronomy Observatories, which are operated by the Association of Universities for Research in Astronomy, Inc., under cooperative agreement with the National Science Foundation.

registration accuracy for the NIC3 fields was less accurate due to the undersampling of the point spread function (PSF) and was of order 0.25 NIC3 pixel ( $0.05''$ ). The NIC3 data were dithered by half-pixel steps to oversample the original pixels by a factor of 2 in the final mosaic. The NIC2 and NIC3 mosaics were rotated to north up and east to the left using the data-header orientation angle and uniformly sampled to  $0.0753''$  square pixels, corresponding to  $0.0029$  pc or  $9.00 \times 10^{15}$  cm at a distance of  $8.0$  kpc. (The pixels are factors of  $1.00906$  (NIC2) and  $1.005$  (NIC3) larger in  $x$  than in  $y$  – this was corrected to make square pixels by interpolation). Where the NIC2 and NIC3 fields overlapped, offsets were determined from centroiding at least 20 common stars in the overlap regions. In the central area covered by NIC2 with better sampling, the final mosaic was made from just the NIC2 pixels.

For the NIC3 images, we employ scale factors of  $5.050 \times 10^{-5}$  and  $5.033 \times 10^{-5}$  Jy (ADU/sec) $^{-1}$  at  $1.87$  ( $P\alpha$ ) and  $1.90 \mu\text{m}$ , respectively (Rieke *et al.* 2003). For the NIC2 images, the scale factors are  $4.086 \times 10^{-5}$  and  $4.330 \times 10^{-5}$ . The rms noise measured in the final NIC3 and NIC2 images in areas of very high extinction with relatively few stars is typically  $3.9$  and  $2.15 \mu\text{Jy}$  per pixel, respectively.

The mosaiced F187N and F190N images are shown in Fig. 1 with a logarithmic stretch on the grey-scale. In the F187N image diffuse emission ( $P\alpha$ ) at the peak level of  $\sim 200 \mu\text{Jy}$  per pixel may be seen; however, over 850 stars in the image are at a level above this brightness. Also apparent in these images are several areas with far lower star counts than their surroundings – presumably due to small but very opaque dust clouds in the line of sight. Contours of HCN (1-0) emission at  $3''$  resolution (Christopher *et al.* 2003) are superposed on the  $1.87 \mu\text{m}$  image; several areas of decreased stellar density are well correlated with molecular clouds seen in HCN (see Fig. 1), implying that the dense dust clouds are located near the Galactic Center as pointed out in an early analysis of this work in Stolovy *et al.* 2001.

### 2.3. Continuum Subtraction and Emission Line Flux Calibration

In order to image the  $P\alpha$  line emission, it is necessary to remove the much stronger stellar point sources. The removal of the stellar continuum from the F187N images is difficult since the stellar density is high, the intrinsic colors of the stars vary and most importantly, the reddening is highly variable across the field. We experimented with three techniques for continuum subtraction (subtraction of fixed-scaled version of the F190N image, point source removal of the stars, and subtraction of a variable-scaled version of F190N) and the results are discussed in the Appendix to this article. The final results

presented below are based on the last technique. A list of emission-line stars is provided in one of the sections below.

To convert the flux densities in the F187N continuum-subtracted image into an emission line flux, we adopted an effective FWHM for the filter of  $190\text{\AA}$  or  $\Delta\nu = 1.63 \times 10^{12}$  Hz.

### 3. $P\alpha$ Images

Fig. 2 shows the  $P\alpha$  emission for the entire region imaged. The reference position of Sgr A\* ( $\alpha_{2000} = 17^{\text{h}}45^{\text{m}}40^{\text{s}}.0383 \pm 0.0007$ ,  $\delta_{2000} = -29^{\circ}00'28.069 \pm 0.014''$ ; Yusef-Zadeh Chaote & Cotton 1999) was located on the NICMOS image using the offsets from maser source IRS 7 given in Menten *et al.* (1997). The relative offsets of all other maser sources specified by Menten *et al.* (1997) (IRS 11NE, IRS 7, IRS 15 NE, IRS 10 EE, IRS 16 NW, IRS 16 NE and IRS 15NE) agreed to within one  $0.0753''$  pixel in the final mosaic image. Subtraction of a scaled F190N mosaic from the F187N mosaic should in principle yield an image of the  $P\alpha$  emission, but, as shown in Fig. 13, strong positive and negative stellar residuals (due to varying intrinsic colors, varying extinction, and photospheric  $P\alpha$  emission and absorption) are apparent. We instead removed the continuum with a scale factor that varied spatially across the field to compensate for these issues as described in the Appendix. This variable spatial scale factor continuum removal method was employed in the subsequent  $P\alpha$  figures and analysis presented here.

The most prominent large-scale emission features in Fig. 2 correspond to : the East-West 'bar' structure approximately  $7''$  south of Sgr A\*, the Northern arm which extends from  $-2''$  to over  $25''$  north of Sgr A\*, and the western arm approximately  $14''$  west of Sgr A\*. With the high resolution and sensitivity of the  $P\alpha$  images, these large-scale features break up into numerous filaments/arcs which are presumably density enhancements in the ionized gas or individual ionization fronts at the edges of neutral clouds. Smaller scale emission peaks are seen on the 26 emission line stars. The 'mini-cavity' appears as a clearly evacuated spherical hole in the emission of diameter  $2.7''$  at  $1.7''$  W,  $2.8''$  S of Sgr A\* (Yusef-Zadeh, Morris, & Ekers 1990) and is as shown in Fig. 2. A weak  $P\alpha$  emission line star appears at the center of this cavity (Stolovy *et al.* 1999). Another weak emission line star is seen at the center of the "eastern cavity" ( $4.6''$  E,  $3.4''$  S).

### 3.1. Extinctions from P $\alpha$ , Radio Continuum and Radio Recombination Lines

The free-free and recombination line emission at radio wavelengths suffer negligible extinction. The observed ratios of P $\alpha$ -to-radio free-free (and recombination line flux) can therefore be used to estimate the dust extinction – both the line and free-free emission depend of the line-of-sight integrated emission measure, but only the P $\alpha$  line emission is significantly extinguished by dust.

For case B recombination, the intrinsic P $\alpha$  flux in a pixel is given by

$$F_{P\alpha} = 6.41 \times 10^{-26} \left( \frac{T_e}{6000K} \right)^{-0.87} \frac{n_e n_p l a_{pix}}{4\pi d^2} \text{ erg s}^{-1} \text{ cm}^{-2} \quad (1)$$

where  $T_e$ ,  $n_e$  and  $n_p$  are the temperature and volume densities of electron and protons,  $l$  is the path length in the ionized gas,  $a_{pix}$  is the projected area of a pixel and  $d$  is the distance (Table 4.4 in Osterbrock 1989; the P $\alpha$  emissivity used to derive the constant in Eq. 1 is appropriate to  $n_e = 10^4 \text{ cm}^{-3}$  but the dependence on  $n_e$  is very weak.) In Eq. 1 and the following, we will adopt  $T_e = 6000 \text{ K}$  (see Morris & Yusef-Zadeh 1989; Simpson *et al.* 1997). Similarly, the radio free-free continuum flux density from a pixel is given by

$$S_{ff} = 4.17 \times 10^{-13} \left( \frac{T_e}{6000K} \right)^{-0.35} \left( \frac{\nu}{5 \text{ GHz}} \right)^{-0.1} \frac{n_e n_p l a_{pix}}{4\pi d^2} \text{ mJy} \quad (2)$$

where  $\nu$  is the frequency of the radio emission. Thus the intrinsic P $\alpha$ /free-free ratio is :

$$\left( \frac{F_{P\alpha}}{S_{ff}} \right)_{intrinsic} = 1.54 \times 10^{-13} \left( \frac{T_e}{6000K} \right)^{-0.52} \left( \frac{\nu}{5 \text{ GHz}} \right)^{0.1} \text{ erg s}^{-1} \text{ cm}^{-2} \text{ mJy}^{-1}. \quad (3)$$

Similar to the radio free-free continuum emission, radio recombination line emission also traces the same ionized gas as P $\alpha$  but suffers negligible extinction, providing an alternative means of estimating the extinction. Roberts & Goss (1993) observed the H92 $\alpha$  recombination line from Sgr A West. If the line is emitted under LTE conditions (Roberts & Goss 1993), then the line flux integrated over the velocity width of emission per pixel is given by

$$S_{H92\alpha} \Delta v = 1.29 \times 10^{-12} \left( \frac{T_e}{6000K} \right)^{-3/2} \frac{\nu}{8.3 \text{ GHz}} \frac{n_e n_p l a_{pix}}{4\pi d^2} \text{ mJy km s}^{-1} \quad (4)$$

using Eq. 13.28 from Rohlfs & Wilson (1996). The intrinsic P $\alpha$ /H92 $\alpha$  ratio is therefore :

$$\left(\frac{F_{P\alpha}}{S_{H92\alpha}\Delta\nu}\right)_{intrinsic} = 4.977 \times 10^{-14} \left(\frac{T_e}{6000K}\right)^{0.63} \left(\frac{\nu}{8.3GHz}\right)^{-1} \text{ erg s}^{-1} \text{ cm}^{-2} (\text{mJy km s}^{-1})^{-1}. \quad (5)$$

The observed flux ratio can be less than that in Eq. 3 and 5 due to extinction at  $\lambda = 1.87\mu\text{m}$  ( $P\alpha$ ). Rieke (1999) derived  $A_{1.60\mu\text{m}}/A_V = 0.176$  and  $A_{2.22\mu\text{m}}/A_V = 0.105$  from NICMOS observations of stars in the Galactic center; interpolating between these values with a  $\lambda^{-1.6}$  power-law yields  $A_V = 7.24 \times A_{P\alpha}$ . (This is nearly equal to the value obtained from Rieke & Lebofsky 1985.) We therefore use the relation

$$A_V = 18.1 \times \log \left( \frac{F_{P\alpha}/S_{ffH92\alpha}^{intrinsic}}{F_{P\alpha}/S_{ffH92\alpha}^{observed}} \right) \text{ mag}. \quad (6)$$

to estimate the visual extinction where  $S_{ffH92\alpha}$  is the free-free or H92 $\alpha$  flux.

To estimate the extinction of the  $P\alpha$  emission, we use the  $\lambda = 6$  cm radio map of Yusef-Zadeh & Wardle (1993). This VLA radio image at  $0.40'' \times 0.67''$  resolution has good sampling at low spatial frequencies; the image therefore contains nearly all the emission on scales corresponding to the CND  $P\alpha$  emission. The  $P\alpha$  image was smoothed to the resolution of the radio image before computing the observed ratios of  $P\alpha$  to radio continuum.

Fig. 3 shows the extinction distribution obtained from the observed ratios of  $P\alpha$  to radio continuum using Eq. 6 and a histogram of the derived extinctions is shown in Fig. 4. The extinctions range from  $A_V \sim 20$  to 50 mag and the median pixel extinction is  $A_V = 31.1$  mag. The median extinction is in good agreement with the median derived from the colors of the Galactic center stars (Blum *et al.* 1996, Cotera *et al.* 2000). However, the extinction exhibits large-scale gradients across the region (see Fig. 3) and low extinctions (20-25 mag) are seen in front of the East-West bar and the Northern arm and in the direction of the IRS 16 cluster. The generally low extinctions seen along the NE-SW swath south of Sgr A\* is consistent with the low extinction values derived for the stellar continuum in IRS 16 (Blum *et al.* 1996). High extinctions (35-45 mag) are seen in the Western arm and in general along the outskirts of the  $P\alpha$  emission. This may be due to the increased extinction associated with dust in the molecular gas along the periphery of the ionized region. The apparently low extinctions toward the  $P\alpha$  emission line stars in the central parsec are contaminated by photospheric excess  $P\alpha$  and should be disregarded in interpreting the line-of-sight extinction in the diffuse gas. The apparently high extinctions shown on Sgr A\* and a few arcsec to the north are spurious, due to the presense of non-thermal radio emission there; the  $A_V$  derived from the H92 $\alpha$  line shows no anomaly on Sgr A\* (see below).

The extinction derived from the 6-cm radio continuum image suffers from two major uncertainties : non-thermal emission and the removal of spatially smooth, low-level emission in the VLA maps. The non-thermal contribution is significant on Sgr A\* and a small contribution could arise from Sgr A East (Pedlar *et al.* 1989). For this reason we also derived the extinction using the H92 $\alpha$  radio recombination line image obtained by Roberts & Goss (1993). This H92 $\alpha$  data, smoothed to 2'' resolution, has a considerably lower SNR (and spatial resolution) than the 6-cm image, but it is completely immune from problems of non-thermal emission contamination by Sgr A\*. Fig. 5 shows the extinction distribution obtained from the observed ratios of P $\alpha$  to H92 $\alpha$  emission using Eq. 6. The areas with sufficient signal-to-noise ratio exhibit extinction values in close agreement with those calculated from the 6-cm data (see Fig. 3). Using the H92 $\alpha$  data, the median pixel extinction is  $A_V = 29.2$  mag, compared with 31.1 mag from the 6-cm analysis (see above). In Fig. 6 we show a histogram comparing the extinction estimates from H92 $\alpha$  and 6-cm radio continuum on a pixel by pixel basis, illustrating the general consistency of the two approaches. Because of the high sensitivity, resolution and spatial coverage, we will use the extinction derived from 6-cm radio continuum in the discussion below, but the agreement between the two methods reassures us that there are not large systematic errors. In addition, the fact that both determinations exhibit a minimum in the ionized bar region and Northern arm argues strongly that this minimum in the extinction is real. Lastly, we note that we also used a 2-cm radio map (Yusef-Zadeh, Morris, & Ekers 1990) for a parallel extinction analysis and derived very similar estimates but this data has lower SNR than the 6-cm data.

### 3.2. Extinction-corrected P $\alpha$ and Lyman Continuum Luminosity

The distribution of P $\alpha$  emission corrected for extinction at 1.87 $\mu$ m is shown in Fig. 7. Although the original radio continuum image is also, of course, extinction-free, the extinction-corrected P $\alpha$  image shown in Fig. 7 has the advantage of higher spatial resolution and signal-to-noise ratio. Under the assumption that the extinction does not vary on scales smaller than the radio image resolution (0.40'' $\times$ 0.67''), this image should provide the most accurate representation of the diffuse HII distribution. A histogram of the derived extinction-corrected P $\alpha$  fluxes (per pixel) is shown in Fig. 8.

The total flux (within 40'' radius of Sgr A\*) in the extinction-corrected P $\alpha$  image is  $2.4 \times 10^{-9}$  ergs cm $^{-2}$  sec $^{-1}$ ; the luminosity is therefore  $1.8 \times 10^{37}$  ergs sec $^{-1}$  or  $1.7 \times 10^{49}$  P $\alpha$  photons per sec. For Case B recombination at 6000 K (Roberts & Goss 1993; Roberts, Goss, & Yusef-Zadeh 1996),  $\alpha_B(H)/\alpha_B(P\alpha) = 22.7$  (Osterbrock 1989) and the total Lyman

continuum (LyC) emission rate required for the  $P\alpha$  emission is  $3.94 \times 10^{50} \text{ sec}^{-1}$  or  $2.70 \times 10^6 L_{\odot}$  (assuming 1.2 Rydbergs per Lyman continuum photon). Within  $20''$  radius of Sgr A\*, the  $P\alpha$  flux is 50% of that given above; thus 50% of the ionizing photons are absorbed within  $20''$  or 0.8 pc. All of the emission line stars are within this region. The derived LyC production rates are *minimum* estimates since we assume Case B recombination with no Lyman continuum escaping the region. Given the apparent geometry of a tilted ring in the neutral gas, it is, in fact, very likely that the actual production rate could be several times higher. The 8 emission line stars studied by Najarro *et al.* (1997) have a combined Lyman continuum emission rate of  $3 \times 10^{50} \text{ sec}^{-1}$  and thus they can probably account for the ionization without any extra input from Sgr A\*. Sgr A\* has not yet been unambiguously identified as an infrared point source in either the continuum or lines. Extended emission is seen in our images at the location of Sgr A\* but no discrete source is seen. The Lyman continuum emission rate obtained from  $P\alpha$  is consistent with that derived directly from the radio continuum ( $\sim 3 \times 10^{50} \text{ sec}^{-1}$ , Genzel, Hollenbach, & Townes 1994).

## 4. Physical Conditions in the Ionized Gas

### 4.1. Sizes of Ionized Structures

The structures seen in the ionized gas are well resolved in the NICMOS  $P\alpha$  images. The emission filaments in the Northern arm and bar have typical FWHM  $\sim 0.3 - 1''$  (or  $0.4 - 1.2 \times 10^{17} \text{ cm}^{-3}$ ) in their small dimension and up to 10 arcsec in their long dimension. The highly elongated, fine structure in the ionized gas is strongly suggestive that the structures are often ionization fronts on the edge of more extensive neutral gas clouds or arms. The ionized shell at the 'mini-cavity' has a diameter of  $2.7''$  or  $3.2 \times 10^{17} \text{ cm}$ . Stolovy *et al.* (1999) discuss the structure of the 'mini-cavity' in  $P\alpha$  and [FeII] emission lines and identify the central star which they propose to be the source of the cavity. The age of the minicavity is only 500 yrs for assumed constant expansion velocities of  $100 \text{ km s}^{-1}$ . It is possibly even a younger structure; Zhao & Goss (1998) estimated a current expansion rate of  $200 \text{ km s}^{-1}$  from radio proper motion measurements.

### 4.2. Electron Densities ( $n_e$ )

Since the extinction-corrected  $P\alpha$  emission is proportional to the volume-integrated emission measure, the electron density in the ionized gas can be obtained from the extinction-corrected  $P\alpha$  image. Inverting Eq. 1, we find :

$$\langle n_e \rangle = 1.21 \times 10^4 F_{P\alpha-14}^{1/2} T_{6000}^{0.44} \frac{D_8}{(l_{17} a_{pix})^{1/2}} \text{ cm}^{-3} \quad (7)$$

where  $F_{P\alpha-14}$  is the line flux in  $10^{-14} \text{ erg s}^{-1} \text{ cm}^{-2}$ ,  $T_{6000}$  is the temperature normalized to 6000 K (Roberts & Goss 1993, Roberts, Goss, & Yusef-Zadeh 1996),  $D_8$  is the distance to the Galactic center (8.0 kpc),  $l_{17}$  is the line-of-sight pathlength (normalized to  $10^{17}$  cm corresponding to  $0.83''$ ), and  $a_{pix}$  is the projected area of the pixel normalized to  $0.0753 \times 0.0753''$ . The peak extinction corrected  $P\alpha$  fluxes along the Northern arm ridge are  $4.3 \times 10^{-14} \text{ erg s}^{-1} \text{ cm}^{-2}$  per pixel. Adopting  $l_{17} = 1$ , the electron density in these peaks is  $n_e = 2.5 \times 10^4 \text{ cm}^{-3}$  and the mean  $n_e$  along the Northern arm is  $n_e \sim 10^4 \text{ cm}^{-3}$ . These estimates are in good agreement with those originally derived by Lo & Claussen (1983) from the radio free-free emission.

### 4.3. Relative Geometry of Ionized and Molecular Features

Some of the large-scale ionized structures can be ascribed to photoionization of the exterior molecular gas by Lyman continuum from hot stars in the central star cluster. The clearest example of this is the Western arm. It extends over  $70''$  (N-S) in both the ionized and molecular gas tracers and the  $P\alpha$  emission centroid is everywhere offset  $5 - 10''$  inside the HCN (Fig. 7). In the western arm, the ionized and molecular gas velocities are also similar (Christopher *et al.* 2003). On the other hand, the ionized structures at smaller radii (e.g. the bar and lower Northern arm) do not have any obvious molecular counterparts. These may be structures which are almost entirely ionized, elongated dynamically and compressed laterally by winds (see below). The north end of the Northern arm in  $P\alpha$  apparently connects smoothly in space and velocity (Lacy, Achtermann, & Serabyn 1991) to a molecular feature extending south ( $\Delta\alpha = 10''$ ,  $\Delta\delta = 30''$ ). In this instance, possibly the neutral gas becomes ionized at  $\Delta\delta \sim 18''$  as it approaches the central cluster. Jackson *et al.* (1993) have suggested that the Northern arm is the ionization front on the surface of an atomic cloud seen in the  $63\mu\text{m}$  [OI] line, which fills the interior of the CND but displays a twin peak morphology similar to that seen in the integrated  $2.12\mu\text{m}$   $\text{H}_2$  emission line (Yusef-Zadeh *et al.* 2001) associated with the molecular torus of the CND. Further evidence for a neutral component of the gas interior to the CND was shown by Stolovy (1997) from [SiII]  $34.8 \mu\text{m}$  observations at  $15''$  resolution, which peaked near the "minicavity" possibly as a result of enhanced Si abundance due to grain destruction in shocks.

Correlation (or lack of correlation) between the molecular gas mapped by the HCN contours in Fig. 3 and the derived extinctions in front of the ionized gas might be used

to infer the relative placement of the H<sub>2</sub> and HII gas along the line of sight. The strong increase in extinction at the edge of the Western arm suggests that some of the ionized gas is behind, or mixed with, the neutral gas and dust in the molecular Western arm. Increased extinction in front of the ionized gas is also apparent where two filaments of molecular gas (traced by the HCN contours in Fig. 3) extend southward into the northern boundary of the ionized gas ( $\Delta\alpha = -5''$ ,  $\Delta\delta = 15''$ , see Fig. 3).

However, Christopher *et al.* (2003) estimate volume densities  $n_{H_2} \geq 10^6 \text{ cm}^{-3}$  for the HCN molecular clouds. Their typical sizes ( $\sim 5''$  or  $7 \times 10^{17} \text{ cm}$ ) then imply column densities  $\sim 7 \times 10^{23} \text{ H}_2 \text{ cm}^{-2}$  or  $A_V \sim 700 \text{ mag}$  for a standard Galactic dust-to-gas ratio. Clearly, the extinctions in front of the the Western arm and northern P $\alpha$  emission are not nearly this high; if they were, no emission would have been detected in the near-infrared. We therefore conclude that P $\alpha$  emission on the west and northern border of the region ( $\Delta\alpha = -10''$ ,  $\Delta\delta = 10''$ ) must be on the front face of the molecular gas (unless the dust is severely depleted or the molecular gas is extremely clumpy on scales  $\ll 1''$ ).

#### 4.4. Tidal Disruption and Stability

The extraordinary small scale structures now seen in both the molecular and ionized gas in the central parsecs, must be extremely short-lived and evolving rapidly. The dynamical time ( $R/V_{rot}$ ) is only  $1.3 \times 10^4$  yrs at  $R = 1.5 \text{ pc}$  with  $V_{rot} = 110 \text{ km s}^{-1}$  (Jackson *et al.* 1993). If some of the ionized gas is infalling at  $\sim 1/2$  of the rotational velocity as suggested by their shapes (for example the Northern arm as modelled by Vollmer & Duschl 2001 and Sanders 1998), then the infall times are only a few  $10^4$  yrs.

Similar short timescales are derived from the small scale structure in the P $\alpha$  emission. Along the Northern arm, the width of the bright emission ridge is just  $10^{17} \text{ cm}$  (corresponding to  $\text{FWHM} = 0.83''$ ); if this gas freely expands at the  $10 \text{ km s}^{-1}$  sound speed of the HII, the time required to double its width is just  $3 \times 10^3$  yrs. Thus if the ionized gas is to maintain its high surface brightness over a dynamical or infall time, the observed emission ridges must be ionization fronts on the edge of dense, neutral material or the ionized gas must be compressed by a much lower density and higher temperature confining medium (e.g. a wind from Sgr A\* or the mass-loss stars – see below) or magnetic fields. Most likely, both scenarios are occurring. The ionized gas on the Western arm is well-correlated both spatially and kinematically with the dense molecular gas seen in HCN emission (Christopher *et al.* 2003) and thus is likely to be the ionized inner face of the molecular arm.

A number of investigations starting with Quinn & Sussman (1985) have emphasized the importance of tidal disruption to the central parsec gas clouds. The Roche limit associated with the central  $2.6 \times 10^6 M_{\odot}$  (i.e. the Sgr A\* black hole; Genzel *et al.* 2000; Ghez *et al.* 2000) is  $n_H \geq 2.4 \times 10^8 / R_{pc}^3 \text{ cm}^{-3}$  (e.g. Sanders 1998). This is a factor of  $10^4$  (!) greater than the density estimated above for the ionized gas in the Northern arm and is comparable to or greater than the densities derived by Christopher *et al.* (2003) for the HCN clumps at  $\sim 2 \text{ pc}$  radius. Inclusion of the mass associated with the stellar distribution doubles the Roche limit at the radius of the CND.

The data clearly show the ionized gas in the Northern arm directly connecting to a N-S feature in the molecular gas. The kinematics of the [NeII] (Lacy, Achtermann, & Serabyn 1991) and HCN emission are also consistent with this connection. Thus, the Northern arm is very likely an infalling streamer originating from the northern molecular gas (Jackson *et al.* 1993, Wright *et al.* 2000). The molecular gas might have been tidally sheared and ionized as it approaches Sgr A\* and the hot central stars.

The sharpness of the Northern arm in cross-section is illustrated in Fig. 9 where a 1-pixel wide slice in the E-W direction is shown for the observed and extinction-corrected  $P\alpha$ . The width is less than  $1''$ . Confinement of the ionized gas in the east-west direction requires a confining medium, magnetic field, or wind ram pressure. Paumard *et al.* (2001) show that there are two classes of emission line stars : those with broad emission lines ( $\Delta V \sim 1000 \text{ km s}^{-1}$ ) and those like the IRS 16 sources with widths of  $\sim 200 \text{ km s}^{-1}$ . The mass-loss stars in the central He cluster have a total  $\dot{M} \sim 3 \times 10^{-3} M_{\odot} \text{ yr}^{-1}$  and typical velocities  $v_w \simeq 750 \text{ km s}^{-1}$  (Hall, Kleinmann, & Scoville 1982; Krabbe *et al.* 1991; Najarro *et al.* 1997). At a distance of  $10''$  (0.4 pc) from the mass-loss stars, the wind will result in a maximum ram pressure  $\rho v^2 \sim 9 \times 10^{-7} \text{ dynes cm}^{-2}$  (assuming no deceleration of the wind). The thermal pressure ( $nkT$ ) of the ionized gas in the Northern arm is approximately two orders of magnitude less ( $8 \times 10^{-9} \text{ dynes cm}^{-2}$  assuming  $n = 10^4 \text{ cm}^{-3}$  and 6000 K). Thus, the mass-loss winds might reasonably contribute to the confinement of the ionized gas in the arm. It is also noteworthy that Baganoff *et al.* (2001) have recently detected X-ray emission from hot, ionized gas in the vicinity of Sgr A\*. This gas could drive an outflowing wind, which might also compress the HII gas in the Northern arm. Aitken *et al.* (1991) concluded from mid-infrared polarimetry that the magnetic field is aligned parallel to the flow of ionized material along the filaments and that the magnetic field is therefore magnified due to these shearing motions. They also concluded that the IRS16 sources do not disturb the magnetic field and therefore they are likely out of the plane of the Northern arm.

Thus, it seems likely that the Northern arm gas must be confined in the E-W direction

by a wind or a confining medium from the general direction of Sgr A\* (but not necessarily from the IRS 16 sources—the IRS13 wind sources and Sgr A\* itself may contribute to the wind). The shape of the Northern arm, concave around Sgr A\*, is also suggestive of pressure confinement on its west side. In the east direction (away from Sgr A\*) the  $P\alpha$  emission in the Northern arm falls off more gradually and hence does not require confinement.

## 5. Candidate $P\alpha$ Emission Line Stars

We used the IDL ‘starfinder’ (Diolaiti *et al.* 2000) program to derive the fluxes in each of the F187N and F190N filters by PSF matching for the NIC2 data only, which led to satisfactory results in deriving stellar fluxes as compared to aperture photometry and scaled PSF subtraction. (The NIC3 portion of the mosaics, despite dithering and resampling of the pixels, did not have sufficiently well defined PSF’s to use PSF-matching techniques). We then correlated well-matched sources found in both filters and computed the F187N/F190N ratios. Although the large width (1%) of the NICMOS F187N filter makes it difficult to detect stars with relatively weak  $P\alpha$  line emission on top of the strong stellar continuum, we do list 26 stars ‘candidate’ emission line stars in Table 2 which were chosen based on derived F187N/F190N flux ratios  $\geq 1.1$ . The typical F187N/F190N ratio for stellar sources was found to be 0.91; a ratio of 1.1 is therefore a conservative indicator of significant ( $\sim 20\%$ ) excess flux at  $1.87\mu\text{m}$ . The high reddening of the Galactic center stars implies F187N/F190N  $< 1$  for all stars. The fluxes in Table 2 have not been corrected for extinction.

The last column in Table 2 lists the likely identification of the stars with previously observed HeI and HI emission line stars (Genzel *et al.* 1996; Najarro *et al.* 1997; Paumard *et al.* 2001). Several of these candidate  $P\alpha$  emission line stars are also strong HeI ( $2.058\mu\text{m}$ ) emission line stars and the F187N flux may indeed be dominated by the HeI line within the bandpass rather than  $P\alpha$ . Some stars in Table 2 appear to be newly identified. (We note that some of the stellar positions listed here disagree with those given by Paumard *et al.* (2001) by as much as  $0.8''$ ; we have discussed this discrepancy with Paumard *et al.* and their revised positions are in better agreement.) We are confident of our positions since the reference stars given by Menten *et al.* (1997) agree to within  $0.07''$  in the NIC2 image. Several stars with high F187N/F190N ratios were removed from the candidate list after visual inspection determined that the excess was dominated by diffuse interstellar  $P\alpha$  emission along the line of sight. Weaker  $P\alpha$  emitters, such as IRS16CC, the ‘minicavity star’, and the ‘eastern cavity star’ do not appear in Table 2, as they do not obey the criterion set by F187N/F190N flux ratios  $\geq 1.1$ . ‘Starfinder’ did not resolve the 2 emission line stars located near IRS13E, now called IRS13E2 and IRS13E4 (Maillard *et al.* 2003).

The fluxes for these stars were derived by a scaled subtraction of the PSF from each star in each filter. IRS15NE appears as 2 stars: a  $P\alpha$  absorption line star to the south coincident with the maser position of IRS 15NE and a star  $0.5''$  to the north, which is an emission line star only imaged in NIC3. Aperture photometry was used to derive the  $P\alpha$  flux for the northern source, which we call IRS 15NNE.

## 6. Centroid and Radial Distribution of Stellar Continuum

It is of interest to determine if Sgr A\* is located near the center of the nuclear star cluster and the ionized gas. Previous ground-based observations of the stellar light distributions have included the contribution from all stars, including the bright stars. Here we investigate the diffuse light surface brightness distribution by measuring the median pixel brightness as a function of radius from Sgr A\* and the mean of pixels excluding the 20% of the pixels with highest brightness. The very clean and stable PSF of NICMOS on HST is particularly advantageous for this analysis. We have also measured the centroids of the total  $P\alpha$  and  $1.9\mu\text{m}$  stellar continuum flux. Although the starlight may not have the same effective foreground extinction distribution as the ionized gas, it is likely the stellar light corrected for the extinction derived for the ionized gas is a much better approximation to the intrinsic  $1.9\mu\text{m}$  continuum than the observed  $1.9\mu\text{m}$  continuum. For the extinction distribution we use that shown in Fig. 3 with the exception that within  $\pm 0.5''$  of Sgr A\*, the extinction was set to the average between  $0.5$  and  $0.75''$  radius which is within 10% of that determined from  $H92\alpha$ . The non-thermal flux of Sgr A\* yields a spuriously high apparent extinction on Sgr A\*. In computing the brightness distributions, we also exclude the very bright source IRS 7. At each radius in the distributions, we only include those pixels within the mosaic area with derived extinctions (and in the case of  $P\alpha$  only those pixels with detected  $P\alpha$ ).

The emission centroids for the total  $P\alpha$  and the  $1.9\mu\text{m}$  flux were measured for apertures of radius 2, 5, 10, 15, 25, 30, 35,  $40''$  from Sgr A\*. These centroids are plotted as boxes in Fig. 10 on top of the  $1.9\mu\text{m}$  image of the region within  $2.5''$  of Sgr A\*. For both the ionized gas and stellar continuum, the centroids remain within  $\pm 2''$  over the entire range out to  $40''$  radius. This provides very strong evidence that Sgr A\* (the putative central black hole) is indeed at or extremely close ( $\leq 0.04$  pc or  $1.2 \times 10^{17}$  cm) to the center of the Galactic nucleus stellar distribution and presumably the dynamical center of the Galaxy.

The radial distribution of observed and extinction-corrected  $1.9\mu\text{m}$  flux density is shown in Fig. 11. We removed the very bright star IRS 7 and the bins in the distributions are independent. The greatest difference between the observed and extinction-corrected

distributions occurs at radii outside  $10''$  where the larger extinction corrections associated with the CNB raise the extinction-corrected flux by a greater amount. The large scale near-infrared light distribution was originally measured by Becklin & Neugebauer (1968) who fitted an  $R^{1.2}$  power-law at radii between  $6''$  and  $10'$ . The extinction-corrected distribution shown in Fig. 11 is clearly somewhat steeper than  $R^{1.2}$  and closer to the  $R^{1.8\pm 0.2}$  power-law shown beside the data. This flux distribution corresponds to a radial density distribution  $\rho \propto R^{-0.5}$  in this outer region. This distribution is considerably flatter than that derived from number counts of individual stars ( $\propto R^{-2}$ , Genzel *et al.* 1996, Allen 1994, Rieke & Rieke 1994). These steeper dispersions are strongly influenced by the 'ring' of early-type and giant stars at radii of  $4\text{--}10''$  (Genzel *et al.* 1996). The outer radial flux distribution (corrected for extinction) is fit by the power law but a noticeable excess flux is seen in the range  $0.8$  to  $10''$  radii in Fig. 11. This excess is probably partially due to the young stars in the IRS 16 cluster.

The mean surface brightness distributions of the *diffuse* starlight are shown in Fig. 12. Here, to avoid the strong effects of bright individual stars, the surface brightness (both mean and median pixel brightness) were computed from the pixels in the lower 80% of the brightness distribution at each radius. (The results are insensitive to the adopted 80% cutoff since cutoff between 50 and 85% were tested with similar results; the 80% cutoff was adopted finally since it makes use of a large fraction of the pixels. The median also attenuates the effects of a few very bright pixels.) Both the observed and extinction-corrected brightness distributions increase at smaller radii but exhibit a sharp drop at  $0.8''$  radius, corresponding to  $0.03$  pc or  $1.0 \times 10^{17}$  cm. To evaluate whether this drop is statistically significant, we independently evaluated the mean and medians for the 4 quadrants (NE, SE, SW, NW) from Sgr A\* and then estimated the uncertainties from the standard deviation of these independent samples – these are the vertical error bars shown in Fig. 12. The central drop is significant given these uncertainty estimates.

The density of discrete stars (as opposed to the total or diffuse light distribution) has been derived as a function of projected radius by Genzel *et al.* (1996). They also found a decrease in the projected surface density of star counts. For stars with  $K \leq 12$  mag, the drop occurs at  $3''$  radius; for brighter star with  $K \leq 10.5$  mag, the decrease occurs inside  $5''$  radius. Thus our results differ significantly from theirs, showing the drop occurring at  $\sim 0.8''$ . Genzel *et al.* (1996) attribute the decrease at small radii as being due to collisions of the giant stars with main sequence stars which then deplete the giant stars because of their relatively large cross-sections.

To test whether the drop in the surface brightness distribution inside  $1''$  is due to a lack of bright giant stars inside  $0.8''$ , we also show in Fig. 12, the median pixel surface

brightness. This median flux should be virtually unaffected by the bright stars which dominate a relatively small fraction of the pixels; it still exhibits a modest decrease at small radii, although not as large as that seen in the mean surface brightness.

The drop or leveling off of surface brightness inside  $1''$  could have several explanations: it might be the core radius of the nuclear stellar distribution or it might be due to the depletion of late type stars with high mass-to-light ratios (Phinney 1989; Bailey & Davies 1999). Gravitational lensing would produce a drop inside the Einstein radius which is on the scale  $0.01''$  (Wardle & Yusef-Zadeh 1992) and is therefore not a likely explanation. Sellgren *et al.* (1990) found a diminishing depth of the  $2.3\mu\text{m}$  CO stellar absorption feature in the central few arcsecs, possibly indicating a depletion of giant stars at the center. An alternative possibility is ejection of stars from the central  $1''$  by a past or present binary black hole (Milosavljevic & Phinney – private communication).

## 7. Summary

We have used a mosaic image of the  $1.87\mu\text{m}$  HI  $P\alpha$  line to estimate the extinction distribution in the Galactic nucleus by comparison with the 6-cm radio continuum and to derive the spatial distribution of ionized gas in the central  $40''$  at  $0.2''$  resolution (Nyquist sampled in the central  $19''$  ).

1) In front of the ionized gas,  $A_V$  varies from 20 to 50 mag with a median pixel value of  $A_V = 31.1$  mag, in excellent agreement with earlier estimates derived for the stellar sources.

2) A broad minimum in the extinction extends  $\sim 30''$  NE–SW over the near the brightest ionized emission (Northern arm, IRS16 region, E-W Bar) and increases in the extinction are seen along the periphery of the ionized gas towards the dense CND molecular features.

3) The minimum Lyman continuum emission rate from within  $40''$  radius of Sgr A\* is  $3.9 \times 10^{50} \text{ sec}^{-1}$  or  $L_{LyC} \simeq 2.7 \times 10^6 L_{\odot}$ . At least half of this emission is within  $20''$  radius.

4) Mass-loss winds from the hot emission line stars are probably responsible for containment of many of the high brightness the ionized filaments.

5) For both the ionized gas and stellar continuum, the centroids of the large scale emission (corrected for extinction derived from  $P\alpha$ ) remain within  $\sim \pm 2''$  of Sgr A\* from  $2''$  out to  $40''$  radius. This provides very strong evidence that Sgr A\* (the putative central black hole) is indeed at or extremely close ( $\leq 0.04$  pc or  $1.2 \times 10^{17}$  cm) to the center of the Galactic nucleus stellar distribution and presumably the dynamical center of the Galaxy.

6) The extinction-corrected enclosed stellar continuum flux is fit quite well by a  $R^{1.8}$  power-law at large radii with an excess from 1 to 8" radius. The  $1.9\mu\text{m}$  surface brightness increases strongly into 1" radius and exhibits a drop with 0.8" of Sgr A\*, possibly indicating the influence of the central black hole on the nearby stellar distribution.

This paper is based on observations with the NASA/ESA Hubble Space Telescope obtained at the Space Telescope Science Institute, which is operated by Association of Universities for Research in Astronomy, Incorporated, under NASA contract NAS5-26555. The NICMOS project was supported by NASA grant NAG 5-3042 to the NICMOS instrument definition team. We thank Doug Roberts for use of his H $2\alpha$  image. It is a pleasure to thank Zara Scoville for assistance in editing.

## 8. Appendix- Stellar Continuum Subtraction

Subtraction of the stellar continuum emission from the  $1.87\ \mu\text{m}$  image was one of the most challenging aspects of this study. Compounding the problem of continuum subtraction from the line+continuum image (F187N), the stellar sources have different intrinsic colors and variable reddening. In addition, some stars have P $\alpha$  emission or absorption.

For subtraction of the stellar continuum from the F187N image, we experimented with three techniques: fixed-scale factor subtraction of F190N from F187N; PSF fitting and subtraction of the stars from the F187N image; spatially variable scale factor subtraction of F190N from F187N. We discuss these approaches separately in the following subsections.

### 8.1. F187N - C $\times$ F190

The most straightforward approach is to multiply the F190N image by a fixed scale factor and subtract this from the F187N image, with the scale factor being that which yields the smallest positive and negative residuals at the locations of identified stars. From trials with the scale factor varying between 0.85 and 1.0 in steps of 0.01, we determined that the best overall scale factor was 0.91 and the resultant residual image is shown in Fig. 13. This scale factor is confirmed in the peak of the histogram of F187N/F190N ratios shown in Fig. 14. The bright positive and negative spots in the residual image are due to too little or too much stellar continuum being subtracted for the individual stars. Positive residuals predominate in the central region, negative residuals near the periphery. This systematic variation clearly indicates that the reddening is lowest in front of the central

area and increases over the periphery. Thus a straightforward subtraction of the F190N image (multiplied by a fixed-scale factor) from the F187N image leaves strong negative and positive residuals at the positions of the stars. This implies that suitable continuum subtraction requires different scale factors at the location of each individual star.

## 8.2. Stellar PSF Subtraction

The second approach removed the stars directly via PSF subtraction. For the PSF fitting we employed the 'starfinder' IDL software package (Diolaiti *et al.* 2000). The software is designed for imaging with oversampled PSFs; thus, PSF fitting was only attempted for the NIC2 mosaic, which only marginally meets this criterion. A composite PSF was derived from the NIC2 mosaic itself and was dominated by the brightest source in the field, IRS7. PSF subtraction was attempted both by subtracting an image of the detected stars (detected fluxes convolved with the PSF) from the F187N directly as well as subtracting stars detected at both F187N and F190N from the fixed scale factor  $P\alpha$  image. We found that PSF fitting with 'starfinder' worked satisfactorily for deriving stellar fluxes in the F187N and F190N images which was used to construct a list  $P\alpha$  emission stars. However, we found that the PSF subtraction of the reconstructed point sources did not give as satisfactory results in removing stellar residuals, possibly due to a non-ideal PSF derivation coupled with the only marginal sampling. This undersampling means that pixelation errors which are quite unpredictable become important. In addition, the strongly varying diffuse  $P\alpha$  background over both small and large scales makes the PSF fitting less accurate than if the field were entirely composed of point sources. We therefore decided after much effort that PSF fitting and subtraction would not yield acceptable results in removing the stellar continuum.

## 8.3. F187N - $C(x,y) \times F190$

Lastly, we experimented extensively with a procedure which determined individual scale factors for approximately 1000 stars identified in the F190N and F187N images, used these scale local factors in the vicinity of each of the stars and then adopted the average stellar scale factor for all remaining pixels. This produced a final residual image, shown in Fig. 2 considerably cleaner than that obtained using a fixed scale factor (Fig. 13), although the procedure involved a number of complex steps.

Specifically, :

1) On both the F187N and F190N images, we first removed the diffuse low-level background ( $P\alpha$  and faint stars) determined as the median intensity in the  $16 \times 16$  pixel area centered on each original  $0.0753''$  pixel. (The value of 16 pixels was chosen to be enough that at least 50% of the pixels would be outside the PSF of bright stars, yet small enough that variations in the background could be picked up.)

2) The F190N pixels associated with each stellar peak were then collected using the algorithm described by Scoville *et al.* 2001. In order to be considered as a star, the peak pixel had to exceed  $410 \mu\text{Jy}$  in the F190N image; and the adjacent pixels were included in the star down to  $175 \mu\text{Jy}$ . Thus the pixel boundaries of over 1500 stars were determined.

3) Local scale factors for *each* star were then derived as the ratio of the total flux measured in the F187N and F190N images within identical pixel boundaries for each star defined from F190N. The derived scale factors for 1031 stars are shown in Fig. 14.

4) An image of the continuum subtraction scale factors ( $C(x,y)$ ) was then made by setting the local scale factor within each star's pixel boundaries to be that derived individually in step 3, and setting the scale factor for all pixels not included in any star to the average of all the stellar scale factors.<sup>2</sup> The use of the 'average' scale factor in the 'non-stellar' pixels does not introduce serious errors – the precise scale factor there makes little difference since the amount of F190N signal which is to be subtracted is lower than the Palpha in F187N in these areas.

5) A difference image was then constructed as  $F187N - C(x,y) \times F190N$ .

6) The difference image was generally better in terms of lower residuals (compared to those in Fig. 13), but still had small residuals near some of the brighter stars (due probably to pixelation errors). Therefore, above the  $410 \mu\text{Jy}$  in the stellar positions, we interpolated from the immediately surrounding pixels.<sup>3</sup>

Although the above process was complex and the last step (# 6) is obviously *ad hoc*, the resulting image retains the maximum areal coverage, replacing only the brightest stellar pixels with interpolated values, and results in an image relatively free of residual stellar effects. The focus of the present paper is the interstellar ionized gas and extinction distributions. The ionized gas in the directions of the stars is clearly more accurately

---

<sup>2</sup>Any stars with apparent F187N/F190N flux ratios greater than 1.1 – a 20% effect since the peak scale factor is 0.91 – were deemed to probably be strong  $P\alpha$  emission line stars (see below); for these stars, the local scale factor was also set to the average scale factor of the remaining stars.

<sup>3</sup>In the vicinity of the very bright star IRS 7 which had a peak continuum surface brightness  $\sim 30,000 \mu\text{Jy}$  per pixel, the area with strong PSF effects ( $30 \times 25$  pixels) was entirely removed and interpolated.

studied with high resolution spectroscopy.

## REFERENCES

- Aitken, D., Smith, C. , Gezari, D., McCaughrean, M., & Roche, P. 1991, ApJ, 380, 419
- Allen, D. A. 1994, in "The Nuclei of Normal Galaxies", ed. R. Genzel & A. I. Harris (Dordrecht:Kluwer), 293
- Bagonoff, F. K., Bautz, M. W., Brandt, W. N., Chartas, G., Feigelson, E. D., Garmire, G. P., Maeda, Y., Morris, M., Ricker, G. R., Townsley, L. K., & Walter, F. 2001, Nature, 413, 45
- Bailey, V. C., & Davies, M. B. 1999, MNRAS, 308, 257
- Becklin, E. E., & Neugebauer, G. 1968, ApJ, 151, 145
- Blum, R. D., Sellgren, K., & DePoy, D. L. 1996, ApJ, 470, 864
- Burton, M. & Allen, D. 1992, PASAu, 10, 55.
- Bushouse, H. A., & Stobie, E. 1998, ADASS, 7, 300
- Christopher, M. H., Scoville, N. Z., Stolovy, S. R., Coker, R. & Yun, M. S. 2003 (in preparation)
- Cotera, A. S., Simpson, J. P., Erickson, E. F., Colgan, S. W. J., Burton. M. G., & Allen, D. A. 2000, ApJ, 129,123
- Diolaiti, E., Bendinelli, O., Bonaccini, D., Close, L. M., Currie, D. G., Parmeggiani, G. 2000, A&AS, 147, 335
- Eckart, A., & Genzel, R. 1996, Nature, 383, 415
- Genzel, R., Crawford, M. K., Townes, C. H., Watson, D. M. 1985, ApJ, 297, 766
- Genzel, R., Hollenbach, D. J., & Townes, C. H. 1994, Rep. Progr. Phys., 57, 417
- Genzel, R. Thatte, N., Krabbe, A., Kroker, H., & Tacconi-Garman, L. E. 1996, ApJ, 472, 153
- Genzel, R., Pichon, C., Eckart, A., Gerhard, O. E., & Ott, T. 2000, MNRAS, 317, 348
- Ghez, A. M., Morris, M., Becklin, E. E., Tanner, A., & Kremenek, T. 2000, Nature, 407, 349

- Güsten, R., Genzel, R., Wright, M. C. H., Jaffe, D. T., Stutzki, J., & Harris, A. I. 1987, *ApJ*, 318, 124
- Hall, D. N. B., Kelinmann, S. G., & Scoville, N. Z. 1982, *ApJ*, 260, L53
- Herbst, T. M., Beckwith, S.V.W. & Shure, M. 1993, *ApJ*, 411, 21
- Jackson, J. M., Geis, N., Genzel, R., Harris, A. I., Madden, S., Poglitsch, A, Stacey, G. J., & Townes, C. H. 1993, *ApJ*, 402, 173
- Krabbe, A., Genzel, R., Drapatz, S, & Rotaciuc, V. 1991, *ApJ*, 382, L19
- Lacy, J. H., Achtermann, J. M., & Serabyn, E. 1991, *ApJ*, 380, L71
- Lo, K. Y. & Claussen, M. J. 1983 *Nature*, 306, 647
- Maillard, J.-P., Paumard, T., Stolovy, S. & Rigaut, F. *Astron. Nachr.*, Vol. 324, No. S1 (2003), Special Supplement "The central 300 parsecs of the Milky Way", Eds. A. Cotera, H. Falcke, T. R. Geballe, S. Markoff (in press)
- Milosavljevic, M. & Phinney, E. S. 2002 (private comm.)
- Morris, M., & Yusef-Zadeh, F. 1989, *ApJ*, 343, 703
- Menten, K. M., Reid, M. J., Eckart, A., & Genzel, R. 1997, *ApJ*, 475, L111
- Najarro, F., Krabbe, A., Genzel, R., Lutz, D., Kudritzki, R. P., & Hillier, D. J. 1997, *Å*, 325, 700
- Osterbrock, D. E. 1989, "Astrophysics of Gaseous Nebulae and Active Galactic Nuclei", University Science Books, (Mill Valley, Ca)
- Ott, T., Eckart, A. & Genzel, R. 1999, *ApJ*523, 248
- Paumard, T., Maillard, J. P., Morris, M., & Rigaut, F. 2001, *A&A*, 366, 466
- Pedlar, A., Anantharamaiah, K. R., Ekers, R. D., Goss, W. M., van Gorkhom, J. H., Schwarz, U. J., & Zhao, J-H 1989, *ApJ*, 342, 769
- Phinney, E. S. in "The Centre of the Galaxy", 1999 ed. M. Morris (Dordrecht:Kluwer), 543
- Quinn, P. J., & Sussman, G. J. 1985, *ApJ*, 288, 377
- Rieke, G. H., & Lebofsky, M.J. 1985, *ApJ*, 288, 618

- Rieke, M. J. 1999 in ASP Conf. Proc. 186 "The Central Parsecs of the Galaxy", 32, ed. H. Falcke, A. Cotera, W. Duschl, F. Melia, & M. J. Rieke.
- Rieke, G. H., & Rieke, M. J. 1994, in "The Nuclei of Normal Galaxies", ed. R. Genzel & A. I. Harris (Dordrecht:Kluwer), 283
- Rieke, M. J. et al. 2003 (in preparation)
- Roberts, D. A., & Goss, W. M. 1993, ApJS, 86, 133
- Roberts, D. A., Goss, W. M. & Yusef-Zadeh, F. 1996, ApJ, 459, 627
- Rohlfs, K., & Wilson, T. L. 1996 "Tools of Radio Astronomy", 2nd ed., Springer-Verlag Berlin
- Sanders, R. H. 1998, MNRAS, 294, 35
- Scoville, N. Z., Polletta, M., Ewald, S., Stolovy, S. R., Thompson, R., & Rieke, M. 2001, AJ, 122, 3017
- Sellgren, K., McGinn, M. T., Becklin, E. E., & Hall, D. N. B. 1990, ApJ, 359, 112
- Simpson, J. P., Colgan, S. W. J., Cotera, A. S., Erickson, E. F., Haas, M. R., Morris, M., & Rubin, R. H. 1997, ApJ, 487, 689
- Stolovy, S. R. 1997 PhD Thesis, Cornell University
- Stolovy, S. R., McCarthy, D. W., Melia, F., Rieke, G, Rieke, M. J., & Yusef-Zadeh, F. 1999, in ASP Conf. Proc. 186 "The Central Parsecs of the Galaxy", 39, ed. H. Falcke, A. Cotera, W. Duschl, F. Melia, & M. J. Rieke
- Stolovy, S. R. , Scoville, N., Yusef-Zadeh, F., & Rieke, M. in Tetons 4: Galactic Structure, Stars and the Interstellar Medium, ASP Conference Series Vol 231, ed. Woodward, Bica and Shull, p. 382
- Thompson, R. I., Rieke, M. J., Schneider, G., Hines, D. C., & Corbin, M. R. 1998, ApJ, 429, 195
- Vollmer, B. & Duschl, W. J. 2001, A&A, 367, 72
- Wardle, M. & Yusef-Zadeh, F. 1992, ApJ, 387, L65
- Yusef-Zadeh, F. Morris, M., & Ekers, R. 1990, Nature, 348, 45
- Yusef-Zadeh, F. & Wardle, M. 1993, ApJ, 405, 584

Yusef-Zadeh, F., Chaote, D. and Cotton, W. 1999, ApJ, 518, 33

Yusef-Zadeh, F, Stolovy, S. R., Burton, M., Wardle, M., & Ashley, M. C. B. 2001, ApJ, 560, 749

Zhao, J.-H. & Goss, W. M. 1998, ApJ, 449, 163

Fig. 1.— The mosaiced F187N and F190N images are shown with pixels sampled to  $0.0753''$  and rotated with north up. The region is dominated by stellar sources, and the  $P\alpha$  emission is seen as relatively faint diffuse emission in the F187N image. The color scale units are  $\mu\text{Jy}$  per  $0.0753''$  pixel and the offsets are relative to Sgr A\* ( $\alpha_{2000} = 17^h 45^m 40^s.058$ ,  $\delta_{2000} = -29^\circ 00' 27.90''$ ). In the  $1.87\mu\text{m}$  image, contours of HCN (1-0) emission are shown and the boxes indicate the positions of the  $P\alpha$  emission stars listed in Table 2. The HCN contours are dashed when negative (i.e. absorption) and the levels are at : -100,-50,-25,-10,-5,2,4,6,8,10,15,20,25,30,35,40,45,50,60 Jy km/ sec /beam.

Fig. 2.—  $P\alpha$  emission for the entire region imaged. The color scale units are  $10^{-16}$  ergs  $\text{cm}^{-2}$   $\text{sec}^{-1}$  per  $0.0753''$  pixel and spatial offsets are relative to Sgr A\*.

Fig. 3.— The extinction distribution derived from the observed ratio of  $P\alpha$  to 6-cm radio continuum emission. The  $P\alpha$  emission was convolved to the same spatial resolution as the radio and we assume the radio continuum is entirely free-free except on Sgr A\*. The contours (-100,-50,-25,-10,-5,2,4,6,8,10,15,20,25,30,35,40,45,50, and 60 Jy  $\text{km s}^{-1}$ ) are for the HCN emission at  $3''$  resolution (Christopher *et al.* 2003). A broad minimum in the extinction is seen in the IRS 16 cluster and the extinctions increase at the periphery of the ionized gas in the molecular features. The dashed contours in the HCN indicate locations where the HCN appears in absorption of the radio free-free (from the ionized gas) and nonthermal (Sgr A\*) continuum. The *apparently* high extinction on Sgr A\* is due to the strong non-thermal contribution which yields spuriously large extinction estimates. Likewise, the interstellar extinction towards the bright  $P\alpha$  emission line stars cannot be accurately measured; the excess photospheric  $P\alpha$  emission yields spuriously low extinction values towards these stars.

Fig. 4.— Histogram of visual extinctions ( $A_V$ ) for pixels with detected radio continuum and  $P\alpha$  emission. The median extinction is  $A_V = 31.1$  mag.

Fig. 5.— The extinction distribution derived from the observed ratio of  $P\alpha$  to H92 $\alpha$  radio recombination line emission (Roberts & Goss 1993). The  $P\alpha$  emission was convolved to the same spatial resolution as the radio ( $2''$ ). The contours are for the HCN emission at  $3''$  resolution (Christopher *et al.* 2003). This extinction distribution agrees closely with that derived independently from the 6-cm radio continuum (Fig. 3). A broad minimum in the extinction is seen in the E-W bar and Northern arm and the extinctions increase at the periphery of the ionized gas in the molecular features. We note that regions with insufficient signal/noise in the H92 $\alpha$  image are masked out (such as the region to the SW of Sgr A\*). The dashed contours in the HCN indicate locations where the HCN appears in absorption of the radio free-free (from the ionized gas) and nonthermal (Sgr A\*) continuum.

Fig. 6.— Histogram of the ratios of extinctions determined from  $P\alpha/H92\alpha$  versus those determined from  $P\alpha/6\text{-cm}$  radio continuum. The histogram is of course restricted to those pixels shown in both Figs. 5 and 3 with determinant extinctions.

Fig. 7.— The  $P\alpha$  emission corrected for extinction using the extinction derived from the ratio of  $P\alpha$  to radio continuum emission (Fig. 3). The color scale units are  $10^{-16}$  ergs  $\text{cm}^{-2}$   $\text{sec}^{-1}$  per  $0.0753''$  pixel and spatial offsets are relative to Sgr A\*. The contours are for the HCN emission at  $3''$  resolution (Christopher *et al.* 2003).

Fig. 8.— Histogram of extinction corrected  $P\alpha$  fluxes (per  $0.0753''$  pixel) for pixels with extinction estimates derived from the ratio of  $P\alpha$  emission to radio continuum.

Fig. 9.— The  $P\alpha$  intensity distribution along an E-W strip (1 pixel wide) crossing the Northern arm is shown. The peak occurs at  $7.2''\text{E}$ ,  $11''\text{N}$  of Sgr A\*. The two traces are for the observed (solid line) and extinction-corrected (dashed line)  $P\alpha$  fluxes.

Fig. 10.— Position centroids of extinction-corrected  $P\alpha$  (small boxes) and extinction-corrected  $1.9 \mu\text{m}$  (large boxes) emissions are plotted on the observed  $1.9 \mu\text{m}$  emission within  $\pm 2.5''$  of Sgr A\*. The centroids were measured successively for pixels within 2, 5, 10, 15, 25, 30, 35,  $40''$  radii of Sgr A\* and each box is labelled with the corresponding radius. The very bright source IRS 7 was excluded and the extinction within  $\pm 0.5''$  of Sgr A\* was set equal to the average in the annulus between  $0.5$  and  $0.75''$  radius (on account of the non-thermal flux of Sgr A\* which precluded extinction estimates directly on Sgr A\*).

Fig. 11.— The radial distribution of observed and extinction-corrected  $1.9 \mu\text{m}$  flux densities are shown as a function of aperture radius. The very bright source IRS 7 was excluded and the extinction within  $\pm 0.5''$  of Sgr A\* was set equal to the average between  $0.5$  and  $0.75''$  radius (on account of the non-thermal flux of Sgr A\* which precluded extinction estimates directly on Sgr A\*). Also shown are an  $R^{1.2}$  power-law which Becklin & Neugebauer (1968) fit to the observed  $2.2 \mu\text{m}$  flux distribution on larger angular scales ( $6''$  to  $10'$ ). The  $R^{1.8}$  power-law fits somewhat better to the extinction-corrected  $1.9 \mu\text{m}$  flux distribution.

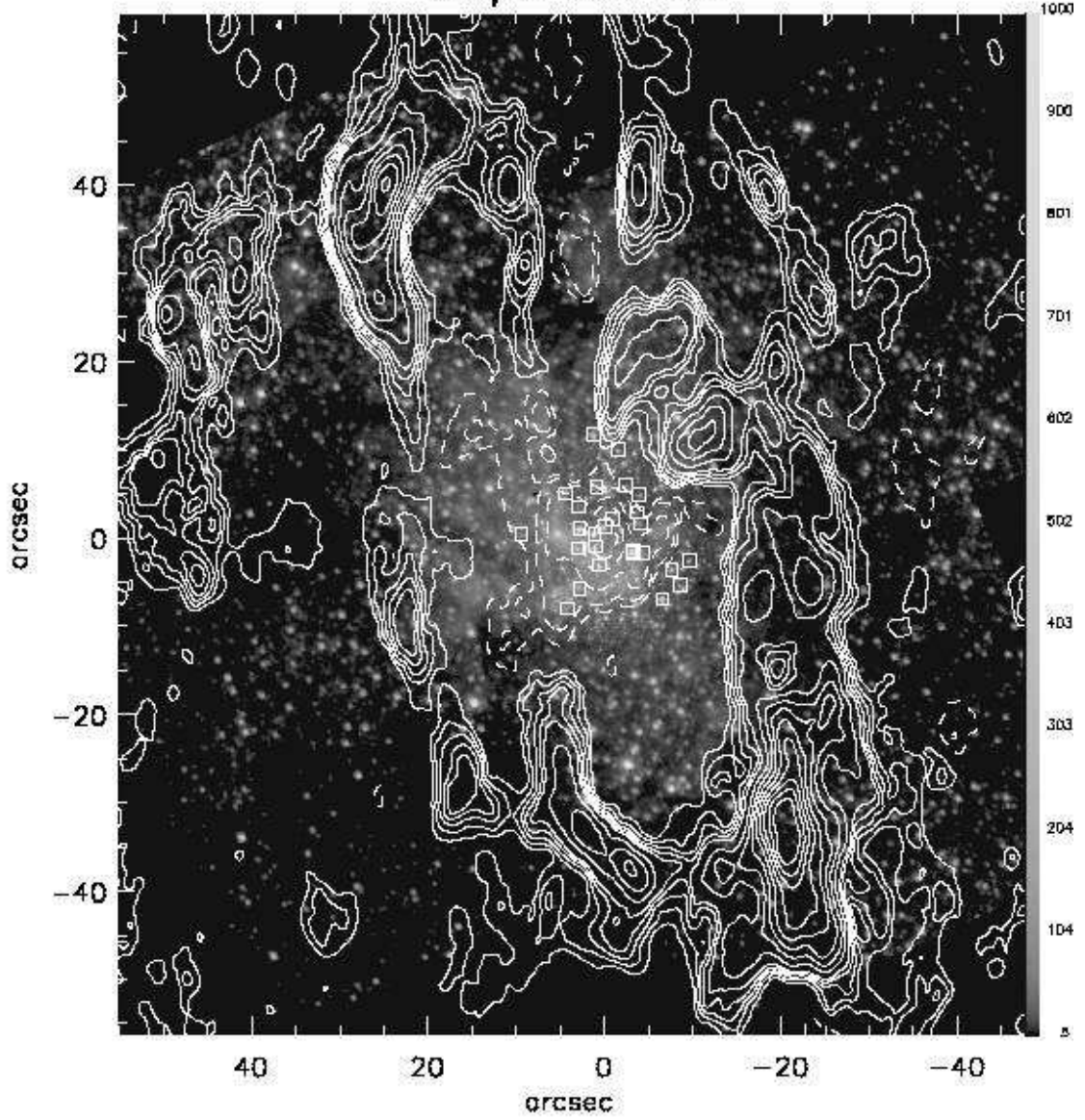
Fig. 12.— The surface brightness distribution for the observed and extinction-corrected  $1.9 \mu\text{m}$  radiation is shown. Discrete, bright sources (such as IRS 7) were excluded by removing the brightest 20% of the pixels in each radial bin. Because the noise is very non-Gaussian (dominated by the stellar brightness distribution), the vertical error bars were estimated from the standard deviation of values calculated in the 4 quadrants relative to Sgr A\*.

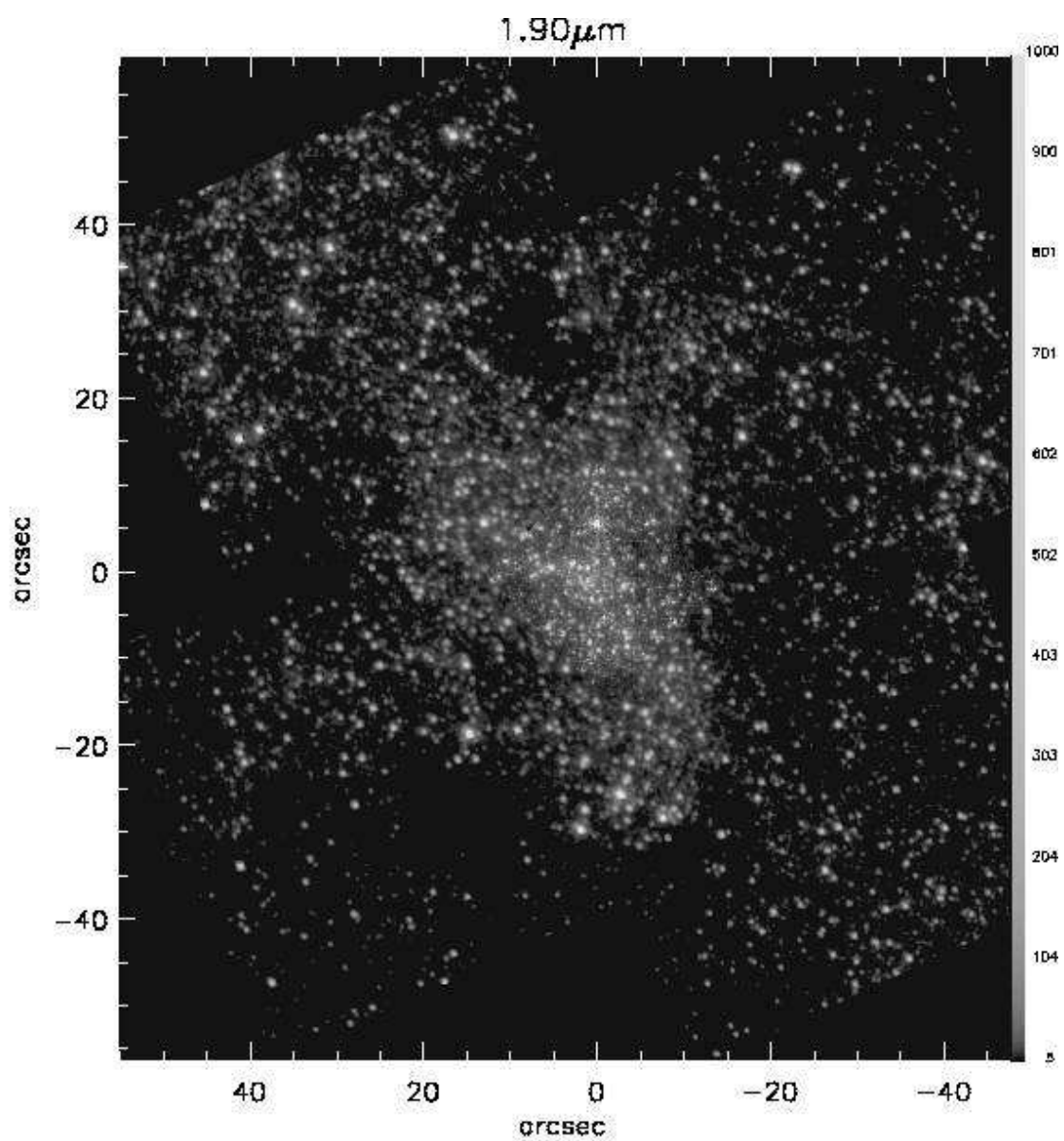
Fig. 13.— The image of  $P\alpha$  emission obtained by subtraction of  $0.91 \times F190\text{N}$  from the F187N image. The bright positive and negative spots in the residual image are due to too little

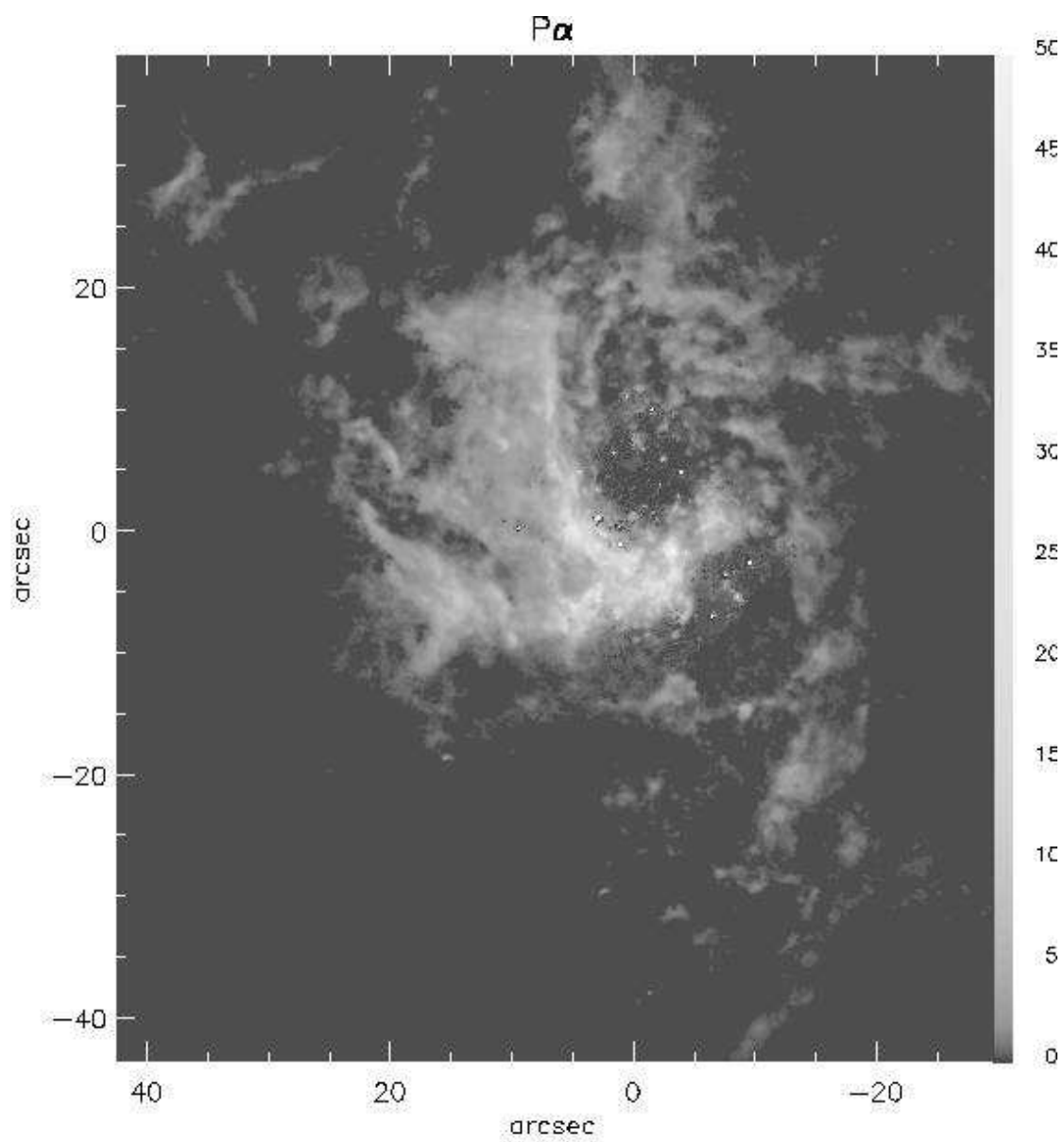
or too much stellar continuum being subtracted for the individual stars. Note that positive residuals are prevalent in the central regions and negative residuals near the periphery – a result of the fact that the reddening is lowest in front of the central area and increases in the periphery. In addition, the  $P\alpha$  emission line stars (see Table 2) are concentrated in the central region.

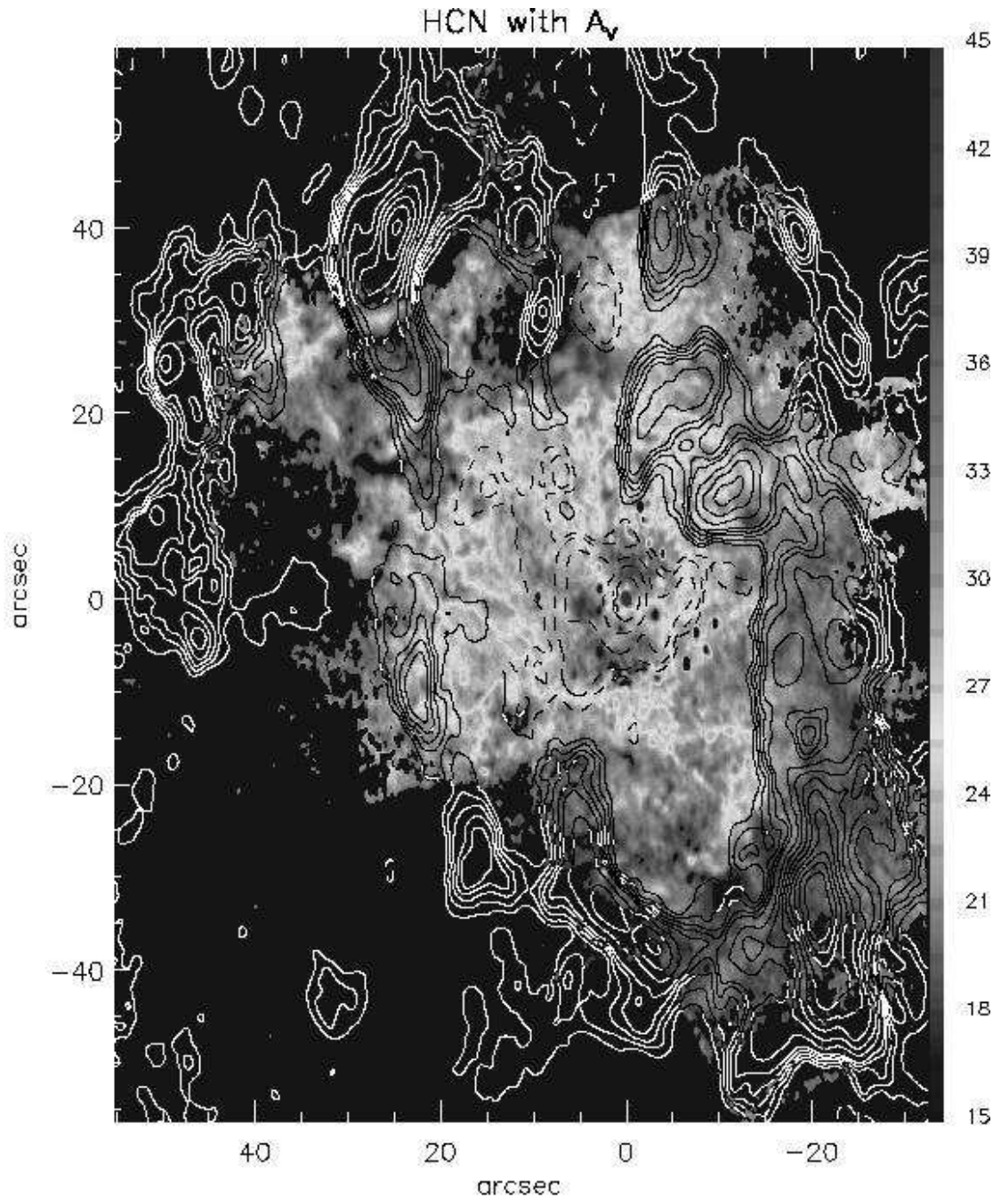
Fig. 14.— The distribution of measured stellar flux ratios  $F187N/F190N$  is shown for 1031 stars determined with the spatially variable scale factor method described in the Appendix.

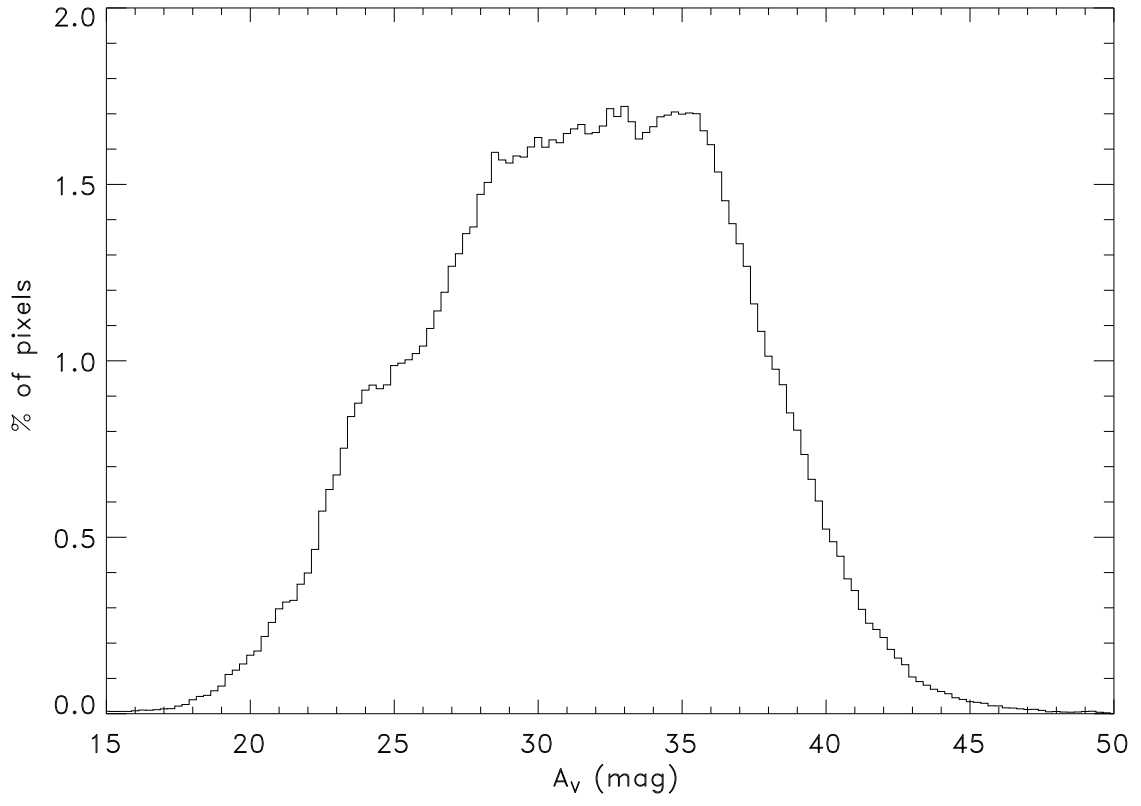
1.87 $\mu\text{m}$  with HCN



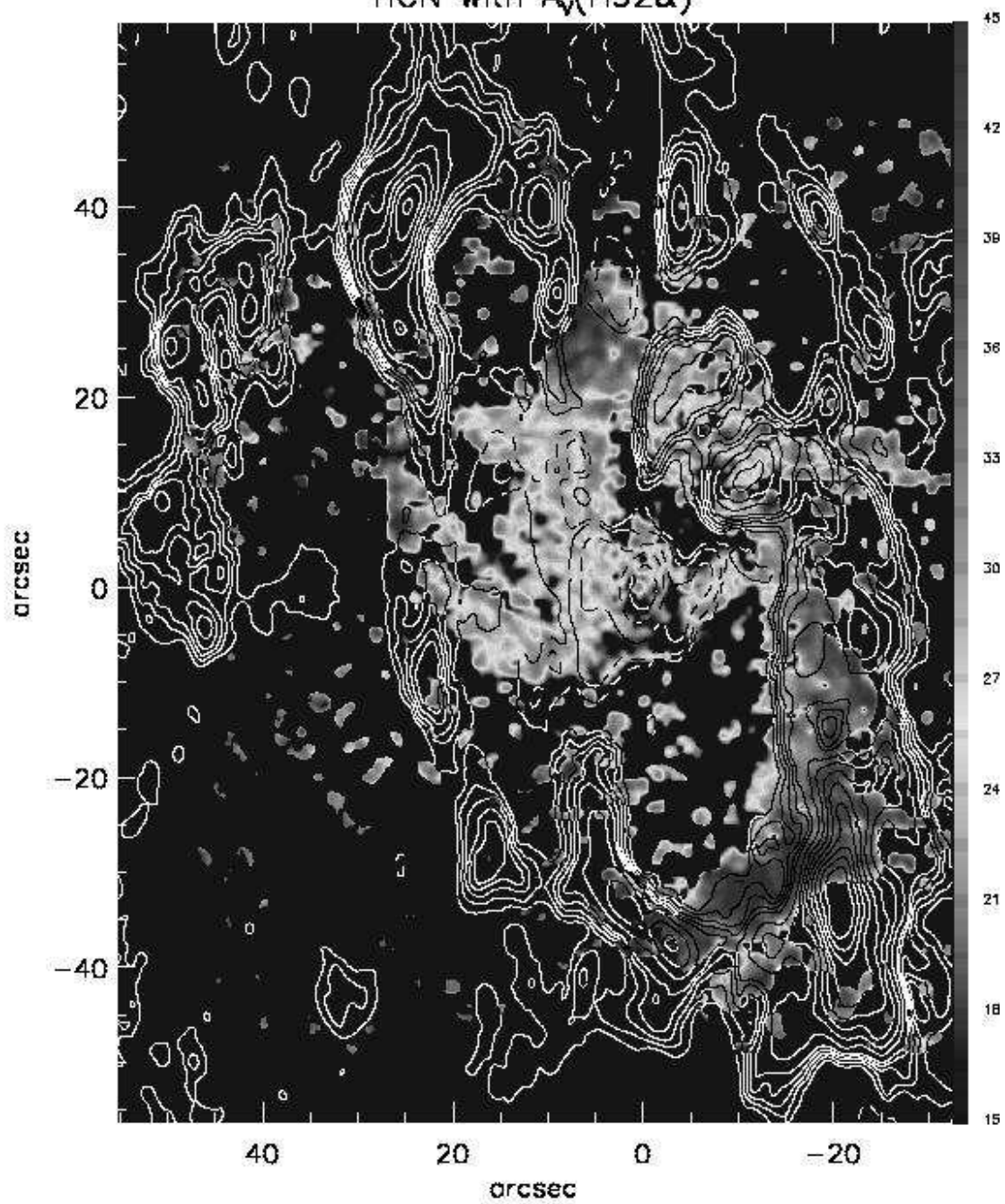


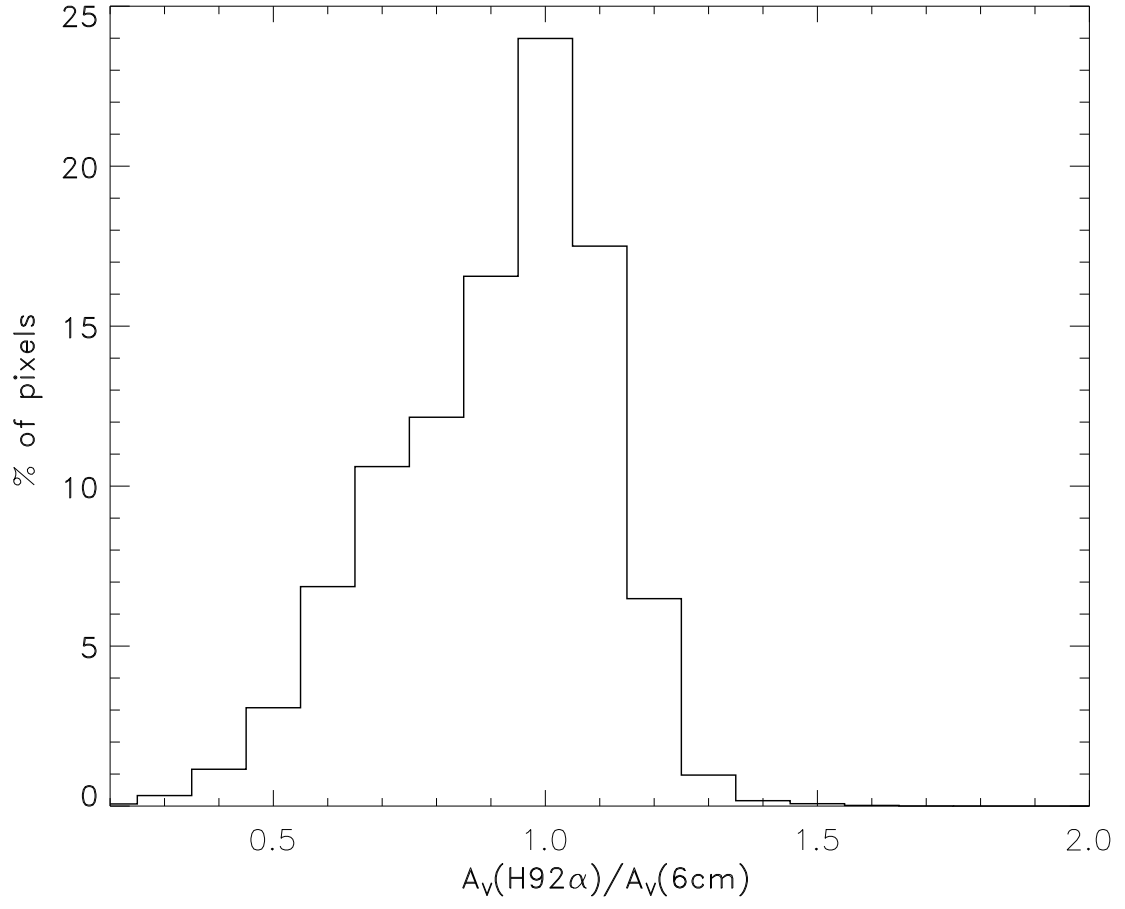


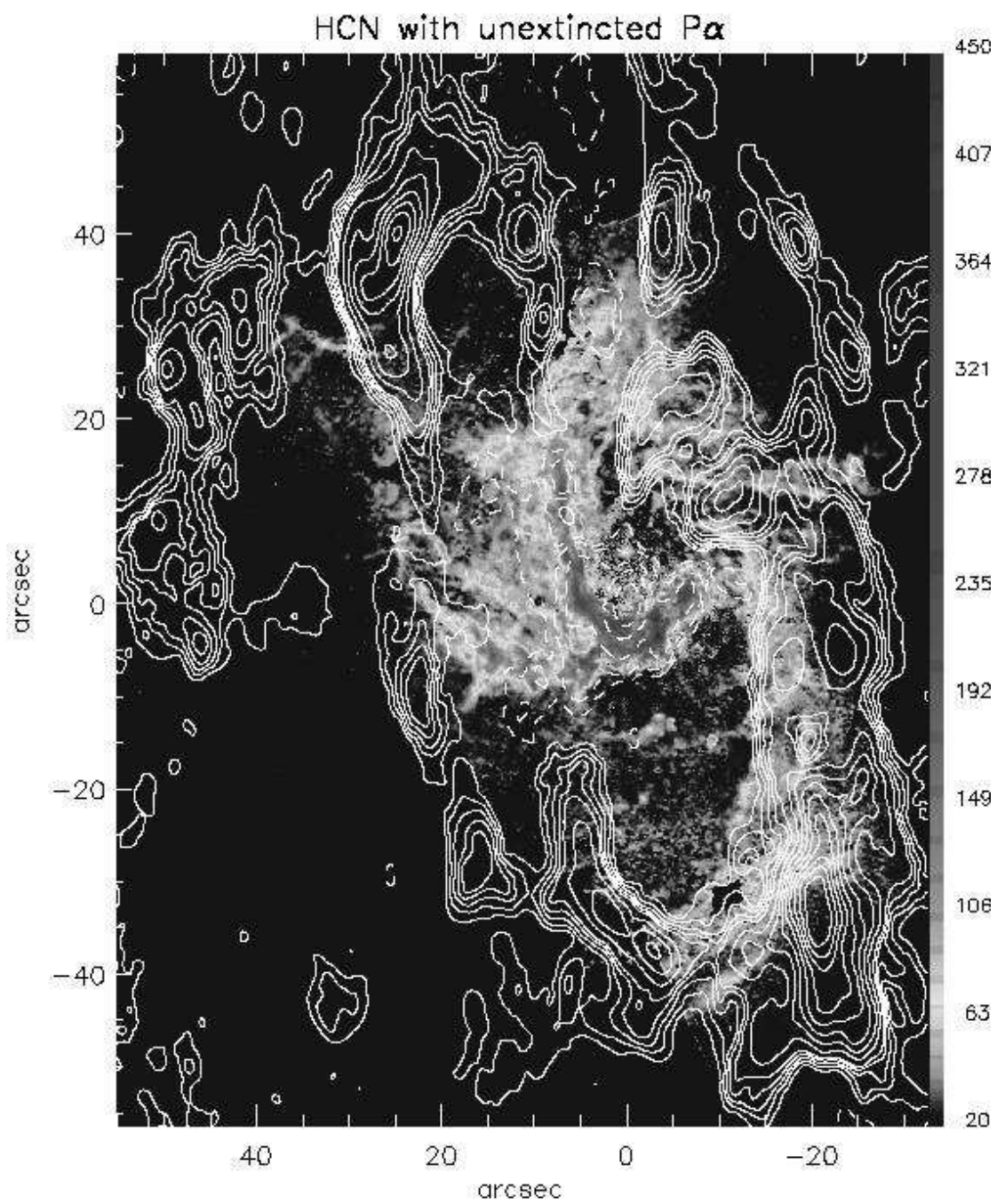


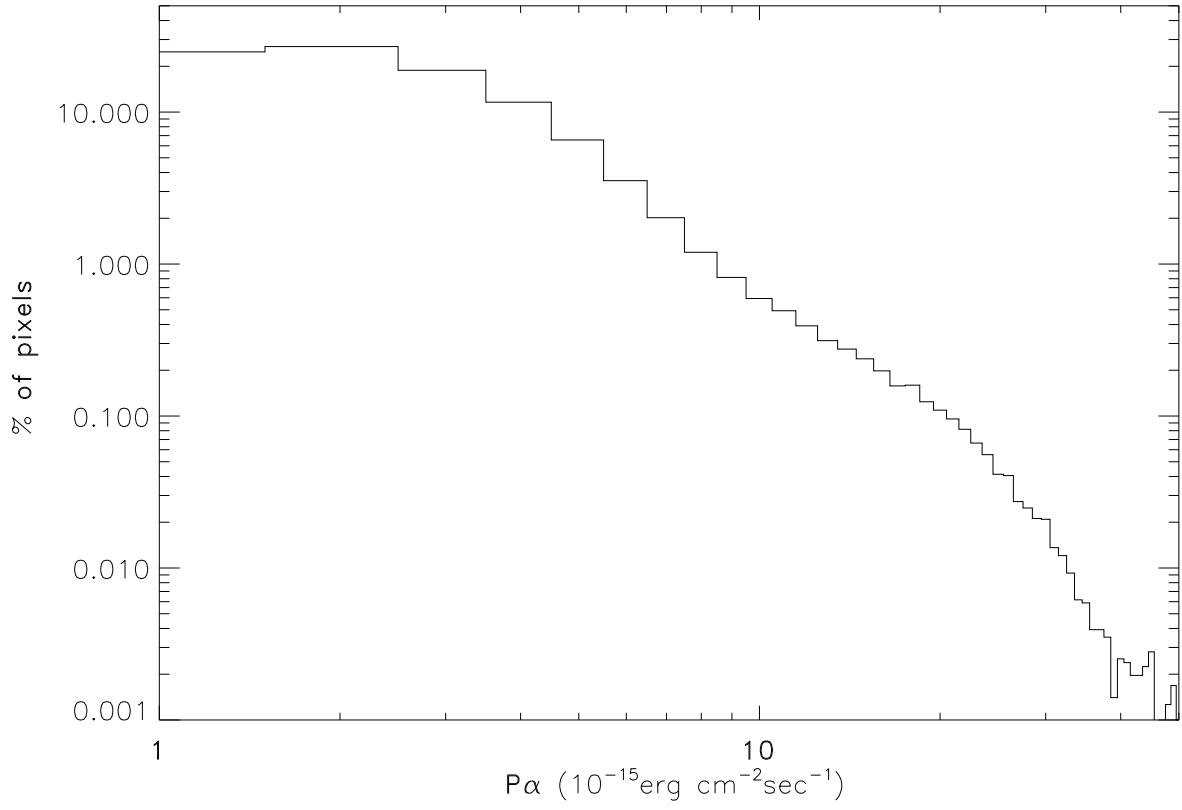


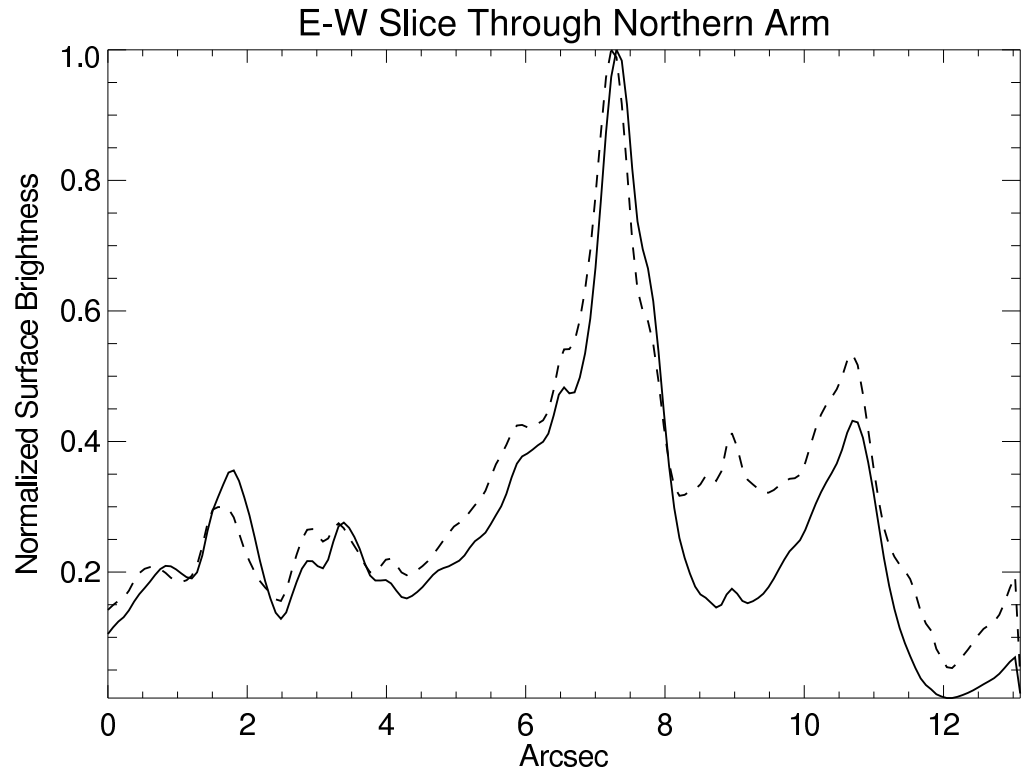
HCN with  $A_V(H92\alpha)$



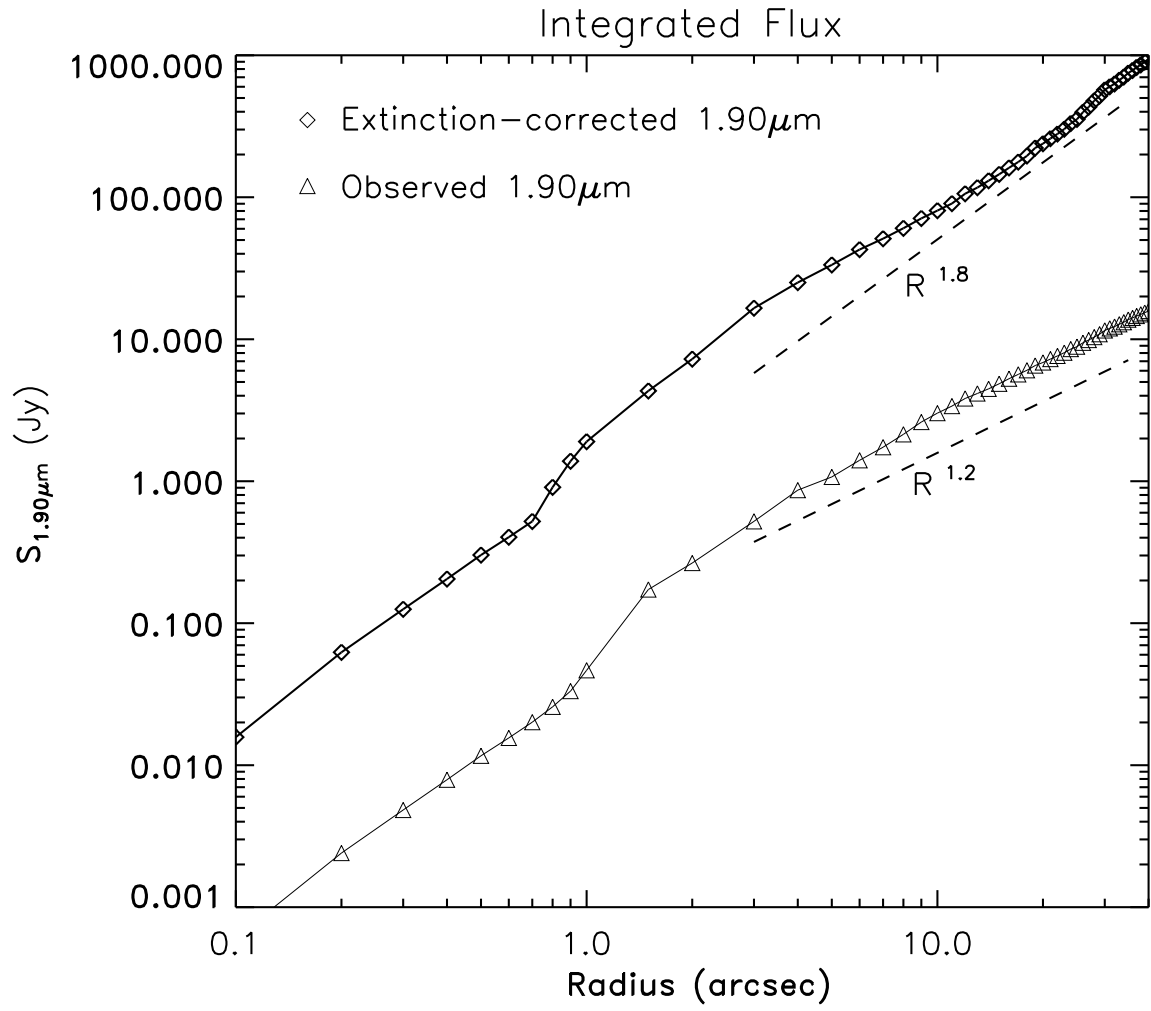


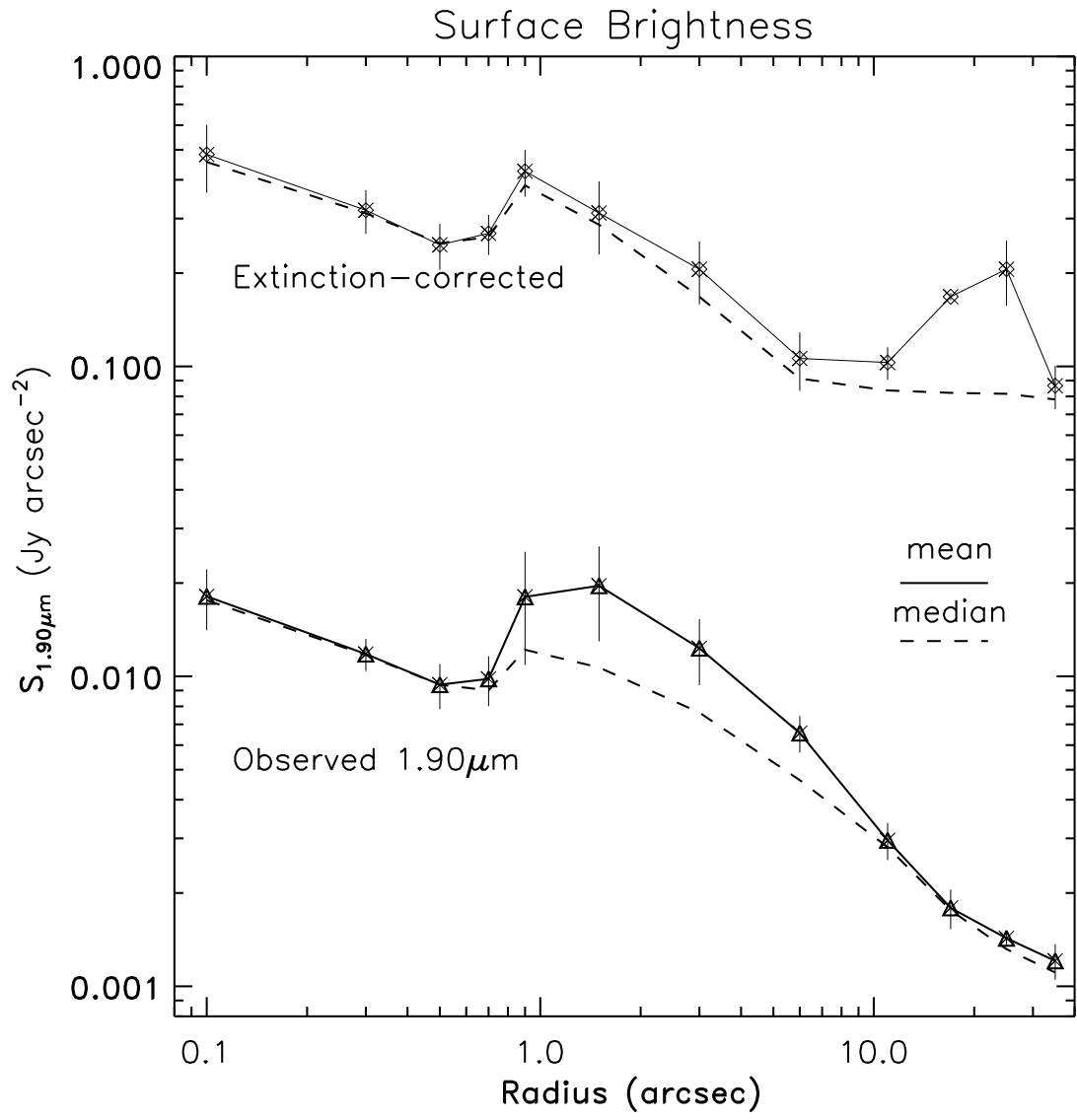


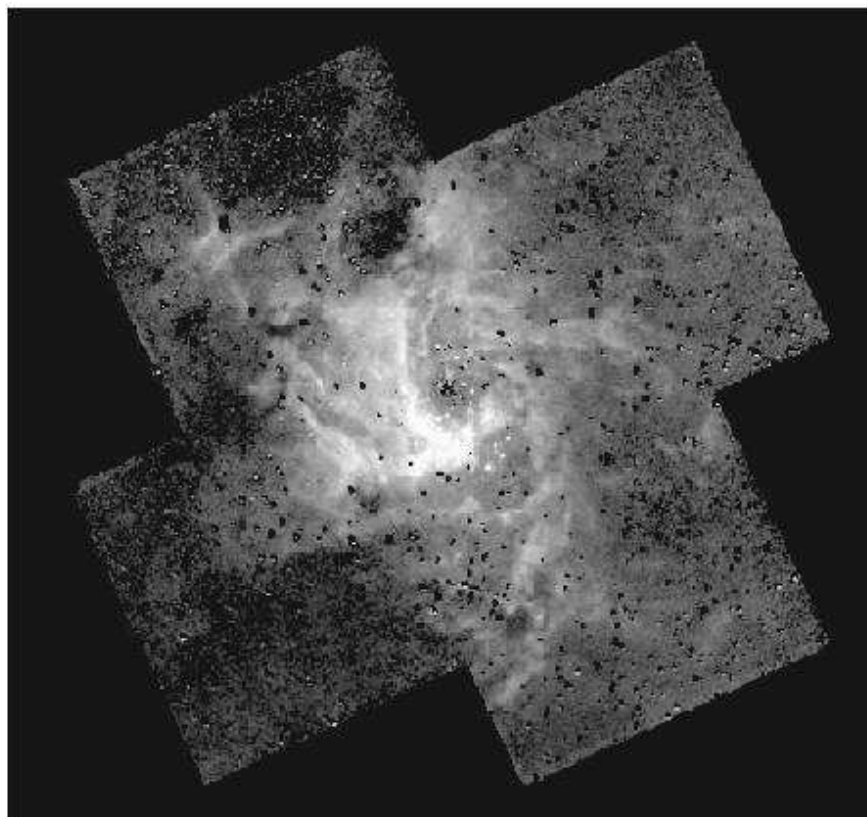












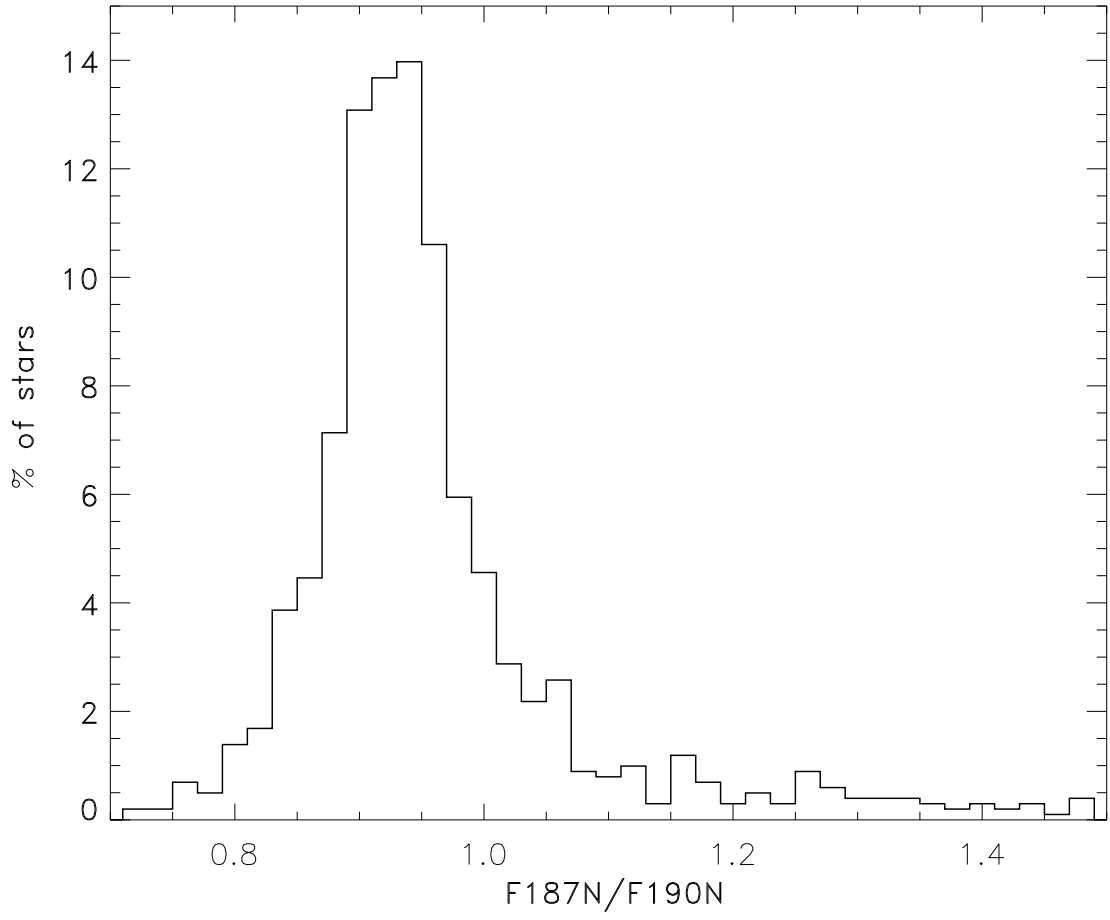


Table 1. Galactic Center P $\alpha$  Observations <sup>a</sup>

Camera	Target <sup>c</sup>	Date	Filter	$\lambda$ ( $\mu\text{m}$ )	Exp. Time (s)	Orient. angle <sup>d</sup>
NICMOS3	GC-A	Apr 6, 1998	F187N	1.874	40 x 4 <sup>b</sup>	24.54
NICMOS3	GC-A	Apr 6, 1998	F190N	1.900	40 x 4	24.54
NICMOS3	GC-B	Apr 6, 1998	F187N	1.874	40 x 4	24.54
NICMOS3	GC-B	Apr 6, 1998	F190N	1.900	40 x 4	24.54
NICMOS3	GC-C	Apr 6, 1998	F187N	1.874	40 x 4	24.86
NICMOS3	GC-C	Apr 6, 1998	F190N	1.900	40 x 4	24.86
NICMOS3	GC-D	Apr 6, 1998	F187N	1.874	40 x 4	24.86
NICMOS3	GC-D	Apr 6, 1998	F190N	1.900	40 x 4	24.86
NICMOS2	GC (center)	Aug 29, 1998	F187N	1.874	304 x 4	223.81
NICMOS2	GC (center)	Aug 29, 1998	F190N	1.900	304 x 4	223.81

<sup>a</sup>All data from Program ID 7250

<sup>b</sup>Four dithers (spaced 1.1" apart in a square pattern) executed for each target

<sup>c</sup>J2000 positions of field centers: GC-A(17:45:41.9,-29:00:04), GC-B(17:45:41.9,-29:00:52),GC-C(17:45:38.1,-29:00:52), GC-D(17:45:38.1,-29:00:04),GC-Center(17:45:40.0,-29:00:28)

<sup>d</sup>Position angle E of N

TABLE 2  
 $P\alpha$  EMISSION LINE STARS IN THE CENTRAL PARSEC<sup>a</sup>

Source	$\Delta\alpha$ (") <sup>b</sup>	$\Delta\delta$ (") <sup>b</sup>	$\Delta r$ (") <sup>b</sup>	F187N/F190N <sup>c</sup>	$m_{F190N}$ <sup>d</sup>	$F_{P\alpha}$ <sup>e</sup>	Identification <sup>f</sup>
1	1.13	0.50	1.24	1.36	10.9	215	IRS 16C
2	0.00	1.24	1.24	1.20	11.0	107	IRS 16NW
3	1.00	-0.94	1.38	1.41	11.0	216	IRS 16SW
4	-0.97	2.09	2.31	1.10	13.3	7	
5	2.85	1.10	3.06	1.23	9.9	329	IRS 16NE
6	2.91	-1.16	3.13	2.59	13.1	126	IRS 16SE2
7	0.61	-3.09	3.15	1.21	11.0	106	IRS 33SE
8	-3.20	-1.43	3.50	2.15	12.7	122	IRS 13E4
9	-3.15	-1.72	3.59	2.07	11.9	236	IRS 13E2
10	-4.05	1.62	4.36	1.36	13.7	15	IRS 34
11	2.92	3.51	4.56	1.62	14.4	14	HeIN3
12	-4.37	-1.64	4.67	1.53	13.6	25	
13	-3.71	2.87	4.70	1.36	14.3	9	
14	0.91	5.81	5.88	1.18	12.7	19	
15	2.81	-5.59	6.26	2.07	13.0	89	IRS 9W
16	-3.95	4.95	6.33	1.63	13.1	47	IRS 7W
17	-2.46	6.01	6.49	1.80	14.3	19	
18	4.41	5.02	6.69	1.84	13.8	32	IRS 7E2
19	-7.63	-3.57	8.42	1.88	12.5	113	AFNW
20	4.22	-7.97	9.02	1.77	14.2	21	
21	9.47	0.37	9.48	1.92	13.6	43	ID180
22	-6.56	-6.92	9.54	3.09	11.0	479	AF
23	-9.64	-2.57	9.98	2.38	13.3	90	
24	-8.64	-5.36	10.17	1.75	13.8	32	
25	-1.53	10.05	10.17	1.78	12.7	81	IRS 15SW
26	1.24	11.81	11.88	1.38	12.0	80	IRS 15NNE

<sup>a</sup>Stars for which the flux in F187N is  $\geq 10\%$  more than in F190N (where the F190N image was multiplied by a factor of 0.91 as discussed in the text)

<sup>b</sup>Offsets and radius are relative to Sgr A\* ( $\alpha_{2000} = 17^h 45^m 40^s .058$ ,  $\delta_{2000} = -29^\circ 00' 27.90''$ ).

<sup>c</sup>F187N/F190N flux ratio

<sup>d</sup>F190N flux density (magnitude), not corrected for extinction; zero magnitude = 808 Jy. All fluxes extracted from NIC2 images using "starfinder" with the exceptions of IRS 13E4 and IRS 13E2 (which required PSF subtraction) and IRS 15NNE (which appears only in the NIC3 image, and for which aperture photometry was performed).

<sup>e</sup>Units :  $10^{-15}$  ergs  $\text{cm}^{-2}$   $\text{sec}^{-1}$ . The fluxes have not been corrected for extinction.

<sup>f</sup>Identifications with stars listed by Genzel *et al.* (2000), Ott, Eckart & Genzel (1999), Paumard *et al.* (2001), and Maillard *et al.* (2003). Our positions were checked against those given by Menten *et al.* (1997) and we find agreement to within  $0.15''$  in all cases.